Progress in Additive Manufacturing
https://doi.org/10.1007/s40964-025-01428-3

RESEARCH

Mechanical properties of additively manufactured AlSi7Mg0.6 and IN718 thin-walled structures

Tim Röver[1] · **Brian Biluh**[1] · **Dirk Herzog**[1] · **Emma Gil**[2] · **Ane Miren Mancisidor**[2] · **Jon Aranzabe**[2] · **M. Belén García-Blanco**[3] · **Elixabete Espinosa**[3] · **Ephraïm Toubiana**[4] · **Leire Arrieta-Lizarazu**[5] · **Joanes Berasategi Arostegi**[5] · **Manex Martinez-Agirre**[5]

Received: 25 February 2025 / Accepted: 6 November 2025

Abstract

Additively manufactured heat exchanger cores offer enhanced compactness, thermomechanical robustness, and improved integration within confined assembly spaces. However, their complex thin-walled lattice structures pose significant challenges for mechanical characterization and conventional finite element analysis, due to high computational costs. This study investigates the tensile mechanical properties of grid-like structures produced by powder bed fusion with a laser beam in aluminum alloy AlSi7Mg0.6 and nickel–chromium-based superalloy Inconel 718 (IN718). Samples with varying wall thicknesses were fabricated, heat treated, and some were surface treated to reduce surface roughness. Tensile tests combined with digital image correlation and non-linear finite element modeling were conducted to evaluate mechanical behavior. Experimental results reveal that a minimum solid material proportion ($P_s \approx 0.09$ for AlSi7Mg0.6; $P_s \approx 0.06$ for IN718) is required to achieve reliable elastoplastic deformation; below these thresholds, premature brittle failure dominates. Equivalent Young's moduli and yield strength scale linearly with solid material proportion, the latter reaching approximately 59% and 52% of bulk material values for AlSi7Mg0.6 and IN718, respectively. Surface treatment contributed mainly to wall thickness reduction without significantly altering mechanical performance. Homogenized porous material models based on the Gibson–Ashby framework and a modified Hockett–Sherby constitutive law were developed, enabling efficient and realistic simulation of these complex structures. These findings provide critical experimental data and modeling tools essential for the design and optimization of next-generation additively manufactured heat exchangers in both alloys.

Keywords Powder bed fusion of metal with a laser beam (PBF-LB/M) · Lattice structures · Thin walls · Mechanical properties · Heat exchanger (HX) · Aluminum alloy AlSi7Mg0.6 · Nickel-chromium-based superalloy IN718 · Surface treatment

1 Introduction

Heat exchangers are essential components for aero gas turbines. They are primarily used for thermal management, functioning as air-cooled oil coolers or fuel-cooled oil coolers for engine oil-cooling, operating at relatively low temperatures [1]. For these applications, aluminum is commonly used, for its lightweight properties [2]. The incorporation of new types of high temperature heat exchangers could enhance the performance of gas turbines, by modifying the thermodynamic cycle [3, 4]. For example, novel recuperators, whose role is to transfer heat from exhaust gas to compressed air, could significantly improve efficiency [3–5]. Likewise, new intercoolers, positioned between the low-pressure and high-pressure compressors, could reduce the work, required to compress air [3, 6]. Additionally, an innovative cooled-cooling air system for compressor bleed could allow for a higher turbine entrance temperature [7, 8] presenting considerable potential to reduce fuel consumption and, therefore, CO_2 emissions. For these high temperature applications, nickel–chromium-based superalloys such as Inconel 718 (IN718) are employed due to their superior

---

Extended author information available on the last page of the article thermomechanical properties. Nevertheless, several issues remain with these heat exchangers, particularly their compactness, integration within the engine, thermomechanical resistance, and weight [2].

Moreover, the increased use of electrical systems onboard and the implementation of geared turbofans will lead to a significant rise in waste heat loads in future aeronautical gas turbines generations [1]. Consequently, it is imperative to develop much more efficient heat exchangers without causing significant increase in fuel consumption.

The rise of Additive Manufacturing (AM) is promising to overcome some of the aforementioned obstacles [9], especially with Powder Bed Fusion of Metals using a Laser Beam (PBF-LB/M) [10]. This technology allows for the production of highly compact and relatively complex components, such as heat exchangers, and facilitates improved integration due to the degrees of freedom offered by the process. Additionally, it could enable enhanced thermomechanical behavior of heat exchangers through a selective material addition to locally reduce the thermomechanical stress during operation. AM permits mechanical reinforcement of critical areas by adding material while keeping the overall material addition to a minimum.

Due to their compactness and lightweight properties, Plate and Fin Heat Exchangers (PFHE) are commonly used in aerospace industry applications such as those mentioned above [11]. These are commonly not produced via AM but manufactured conventionally using e.g. brazing [12]. Thermomechanical studies and creep fatigue life prediction are critical for PFHE when operating at high temperatures and pressures in addition to thermal cycling. However, these heat exchangers often consist of more than a hundred thousand fins, making stress analysis via the conventional Finite Element Method (FEM) very demanding in terms of computational resources. An effective analysis approach is to consider PFHE structures as porous structures and then use the homogenization method [13–18] to calculate the equivalent material properties and the equivalent stresses. The homogenization method is based on earlier works [19–24]. However, the aforementioned studies on PFHE focus on conventionally manufactured heat exchanger cores and not AM heat exchangers.

Although the use of AM comes with a great potential for improvement of heat exchangers, certain aspects must be considered regarding its use for this application. As stated previously, next-generation heat exchangers must be highly efficient, meaning their thermal and fluid flow performance must be optimized. Furthermore, component weight must be minimized while ensuring structural integrity under operating conditions. To reduce the weight of a given heat exchanger, a major lever is to minimize the heat exchanger's wall thickness. However, achieving wall thicknesses at the limits of the state-of-the-art of PBF-LB/M implies that internal defects, surface roughness, and microstructure could significantly impact the resulting macroscopic mechanical properties. Defects such as pores and lack of fusion are common issues in the PBF-LB/M process [25–27]. Spatter ejection, keyholing, and lack of fusion can lead to void formation during the PBF-LB/M process. Voids of irregular shape, caused by lack of fusion, result in higher stress concentrations than spherical voids or pores. They thus exert more influence on the mechanical properties, such as material failure, by promoting crack initiation and crack propagation [28]. Nevertheless, these lack of fusion-defects can often be prevented by optimizing the processing parameters. Multiple studies on thin-walled additively manufactured structures linked to the previously mentioned aspects are introduced later in this chapter. Furthermore, surface roughness was identified as a key parameter for the thermal and fluid flow characteristics of additively manufactured metal heat exchangers [9] which must be considered in the design of these components.

In development of AM heat exchangers, information about the macroscopic mechanical response of heat exchanger cores is needed. Thin-walled grid like core structures are of interest for a new-generation of heat exchangers that are based on a layered flow setup (more information will be given in the subsection Sample design). Empirical data and suitable material models are needed to allow for an efficient design of these components. Additionally, surface roughness of the manufactured thin-walled core structures is of high relevance for the application.

Despite the clear need for detailed information on the macroscopic mechanical properties of thin-walled, grid-like structures manufactured via PBF-LB/M in aluminum alloy AlSi7Mg0.6 and nickel–chromium-based superalloy IN718, such targeted data remain scarce in the literature. A thorough review reveals that existing studies addressing thin-walled structures in these materials largely focus on different geometries or emphasize microstructural, process parameter, or compressive behavior aspects without directly investigating tensile mechanical performance of grid-like cores.

Starting with aluminum alloys, some studies have addressed thin-walled or lattice structures produced by PBF-LB/M. For instance, Yuan et al. [29] examined thin-walled grid-like structures in AlSi10Mg, focusing mainly on process parameters, melt pool temperatures, and micro- and nano-hardness distribution. They observed enhanced hardness in intersection areas due to finer microstructures. Subsequently, the same group investigated larger grid structures with an emphasis on their optical focusing capabilities [30], rather than mechanical properties. While these structures bear geometric similarity to those studied here, they pertain to AlSi10Mg rather than AlSi7Mg0.6, and do not provide macroscopic mechanical characterization.

Focusing on AlSi7Mg alloys, Wan et al. [31] produced thin-walled components with wall thicknesses of 0.6 mm and 1 mm, investigating their application as vibration isolators rather than heat exchanger cores. Similarly, Mantovani et al. [32] analyzed body centered cubic lattices with x-, y-, and z-struts (BCCxyz) fabricated in AlSi7Mg, concentrating on compressive stiffness, strength, and energy absorption, but such strut-based lattices cannot separate fluid flows as required in heat exchanger cores. Recent work by Bogahawaththa et al. [33] evaluated fractal porous structures in AlSi7Mg via PBF-LB/M, identifying superior energy absorption compared to honeycomb or gyroid geometries and validating Gibson–Ashby predictions for elastic stress; nonetheless, their fractal topologies differ significantly from grid-like applications. Likewise, Zhang et al. [34] explored uniform and graded gyroid structures for energy absorption, noting enhanced performance with grading, but their architecture and functional intent diverge from heat exchanger cores.

Additional studies investigated single thin walls with thicknesses between 0.1 mm and 0.8 mm manufactured from AlSi7Mg, assessing the effects of heat treatments on density, microstructure, and low-cycle fatigue resilience [35]. Furthermore, Liu et al. [36] studied Triply Periodic Minimal Surface (TPMS) structures in AlSi7Mg0.6 focusing on heat dissipation rather than mechanical properties, while Richter et al. [37] analyzed self-heating effects in thermomechanical deformation of PBF-LB/M AlSi7Mg0.6 dog bone samples, correlating experiments and numerical models. Collectively, despite advances in porous, lattice, and thin wall investigations, there is a noticeable lack of focused research on the macroscopic tensile mechanical behavior of thin-walled grid-like AlSi7Mg0.6 structures relevant to heat exchangers.

Turning to IN718, a range of studies evaluates thin-walled or lattice structures fabricated by PBF-LB/M, though most emphasize honeycomb, TPMS, or strut-based lattice geometries rather than grid-like arrays. Pérez et al. [38] and Voyiadjis et al. [39] investigated process influence on wall thickness, microhardness, and compressive strength in honeycomb IN718 structures, concluding that contour scanning enhances accuracy and reduces manufacturing time but without addressing grid-like tensile behavior. Xu et al. [40], Pauzon et al. [41], and Majeed et al. [42] explored gyroid lattices in IN718, analyzing compressive and fatigue responses, microstructure, and heat treatment effects, with Pauzon et al. [41], additionally linking processing parameters and microstructural features to mechanical performance. Srivathsan et al. [43] compared TPMS and strut lattices, demonstrating superior ultimate compressive strength in gyroid and diamond structures at equivalent relative densities.

Strut-based lattices in IN718 have been further characterized by Ananda et al. [44] and Banait et al. [45], where tensile testing revealed effective moduli while microstructural examination highlighted marked differences between PBF-LB/M lattices and bulk materials due to rapid solidification. Other important work on thin-walled, non-lattice IN718 components includes studies on stator vanes [46], tubular components [47], and manufacturability challenges of ~ 0.2 mm walls [48]. Residual stress analyses in thin walls, including their impact on elastic properties, were conducted by Ahmed et al. [49] and Wu et al. [50]. These studies showed that thinner walls exhibit more distortion but lower residual stresses, which can be mitigated by strategic material addition.

Mechanical testing remains a focus in several works: Wang et al. [51] demonstrated how parameter optimization and heat treatment in 1 mm thick tensile specimens strengthen IN718 PBF-LB/M parts, with strengths reaching 1570 MPa at 27.3% elongation. Investigations of fracture behavior in ~ 0.5 mm thin walls by Golinveaux et al. [52] highlighted that heat treatment and hot isostatic pressing generally reduce fatigue life compared to as-built samples, while Varney et al. [53] compared mechanical properties between thin walls manufactured directly and those extracted from bulk IN718, noting greater variability and influences of microstructure and surface roughness in the former.

Despite these extensive studies, thin-walled IN718 investigations predominantly emphasize honeycomb, TPMS, and lattice architectures. Tensile mechanical characterization of grid-like configurations akin to heat exchanger cores remains underexplored. These existing works collectively underscore the vital of process conditions, heat treatments, microstructure, residual stress, and surface finish on mechanical performance but also highlight the pressing need for focused research on tensile response of thin-walled grid-like structures in both AlSi7Mg0.6 and IN718.

Regardless of the growing body of research on thin-walled structures manufactured from AlSi7Mg0.6 and IN718 via PBF-LB/M, there remains a significant gap in understanding the macroscopic mechanical behavior of thin-walled, grid-like structures crucial for certain heat exchanger applications.

This article aims to address this knowledge gap by providing comprehensive empirical data based on uniaxial tensile tests and material modeling tailored to these specific geometries and materials. Filling this gap is essential to enable the efficient and reliable design of next-generation additive manufactured heat exchanger cores.

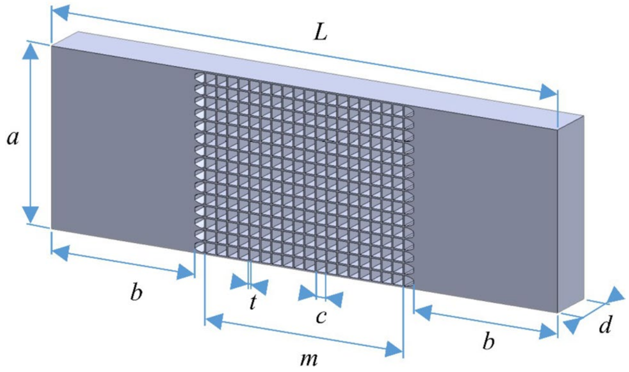

Fig. 1 Parametric sample geometry of the samples that were investigated in this study

Building on the identified need for comprehensive mechanical property data and suitable material models for thin-walled, grid-like structures manufactured via PBF-LB/M in AlSi7Mg0.6 and IN718, this study undertakes a systematic experimental and numerical investigation. The following section details the design, manufacturing, post-processing, and characterization of tensile test samples developed to emulate heat exchanger cores, along with the experimental uniaxial tensile testing protocols and finite element modeling approaches used to evaluate their mechanical behavior. The subsequent section presents the experimental results based on uniaxial tensile tests, compares them with numerical predictions, and introduces homogenized material models based on the Gibson–Ashby framework and a modified Hockett–Sherby constitutive law to enable efficient and accurate simulation of these complex structures.

2 Methods and materials

In this section, the used methods and materials are presented.

2.1 Sample design

Figure 1 shows the parametric sample geometry used for this study. The samples consist of clamping areas and the thin-walled grid structures. The grid structure represents the heat exchanger core in a counterflow configuration, featuring a layered flow setup. In this design, the grid walls aligned in one direction represent parting walls, which separate the hot and cold fluid layers within the heat exchanger core, while the grid walls oriented in the perpendicular direction represent fins.

Geometrical characteristics of experimental samples and simulation samples can be found in Tables 1 and 2, respectively.

For each of the two materials eight surface-treated sample types and four untreated sample types were considered with three samples per sample type. Therefore, the design of experiment consisted of a total number of 72 experimental

Table 1 Range of geometric parameters of experimental sample designs. For individual values per sample batch, the reader is kindly referred to the appendix

	Avg. channel size c_{mean} [mm]	Avg. wall thickness t_{mean} [mm]	Total cross-sectional area (including voids) A_T [mm^2]	Cross-sectional area of thin walls (excluding voids) A_{tw} [mm^2]	Proportion of solid material in majorities of cross-sectional areas $P_s = A_{tw}/A_T$
AlSi7Mg0.6					
Non-surface-treated	1.816…2.023	0.206…0.353	322.04…366.52	34.61…59.19	0.1075…0.1618
Surface-treated	1.890…2.167	0.089…0.225	317.10…361.71	14.80…37.44	0.0467…0.1069
IN718					
Non-surface-treated	1.906…1.993	0.110…0.303	312.79…350.18	18.18…48.87	0.0573…0.1396
Surface-treated	1.870…2.034	0.080…0.258	302.15…347.09	12.65…41.36	0.0417…0.1192

Table 2 Geometric parameters of finite element analysis sample designs

	Channel size c [mm]	Cross-sectional area (including voids) A_T [mm^2]	Cross-sectional area of thin walls (excluding voids) A_{tw} [mm^2]	Proportion of solid material in majorities of cross-sectional areas $P_s = A_{tw}/A_T$
AlSi7Mg0.6				
Wall thickness $t = 0.15$ mm	2	324	24	0.0741
Wall thickness $t = 0.25$ mm	2	340	40	0.1176
Wall thickness $t = 0.30$ mm	2	348	48	0.1379
IN718				
Wall thickness $t = 0.15$ mm	2	324	24	0.0741
Wall thickness $t = 0.25$ mm	2	340	40	0.1176
Wall thickness $t = 0.30$ mm	2	348	48	0.1379

Table 3 Chemical composition (wt%) of AlSi7Mg0.6 and IN718 powders used for the manufacturing of samples via PBF-LB/M

Powder	Al	Fe	Ni	Si	Cu	Mn	Mg	Zn	Ti	Cr	Mo	Nb	Co	Ta
AlSi7Mg0.6	Bal	0.12	–	6.6	0.001	0.003	0.63	0.002	0.041	–	–	–	–	–
IN718	0.58	Bal	54.4	0.032	0.007	0.022	–	–	0.92	18.8	3.09	5.17	0.035	<0.005

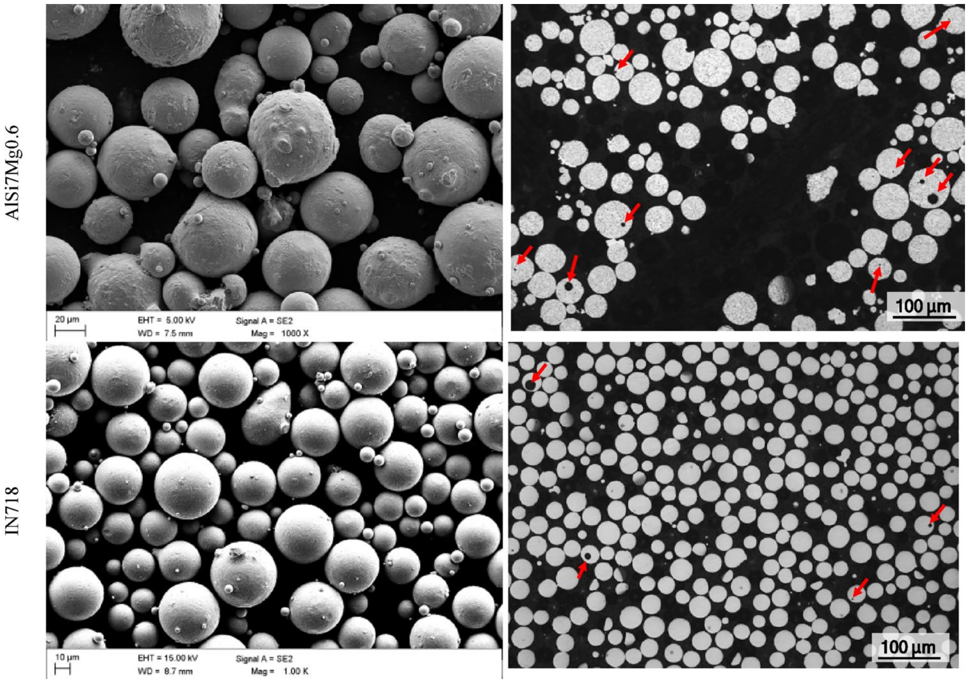

Fig. 2 AlSi7Mg0.6 and IN718 powders characterization. AlSi7Mg0.6 (top) and IN718 (bottom) powders micrographs showing its (left) morphology and (right) internal porosity pointed out with red arrows

samples. Additional geometrical data regarding the experimental samples can be found in Appendix Table 10.

The target channel size for the designs was 2 mm. Data from Table 2 aligns with the CAD-files of the samples. With regard to Table 1, parameters L, b, m and A_T are according to the CAD-files of the samples. Parameters a, d and t_{mean} were measured by caliper on the manufactured samples. Parameters c_{mean} and A_{tw} are based on t_{mean}, a and the CAD-file. The solid material proportion (P_s) is based on A_{tw} and A_T and values for the experimental samples can be found in Appendix Table 10. Parameter P_s refers to the relevant cross-sectional area of the samples and its definition is given in the following. The presented samples have two relevant types of cross-sectional areas:

(1) Cross-sectional areas located at the nodes of the grid, which are perpendicular to the tensile test direction. These areas consist entirely of solid material (proportion of solid material in cross-sectional area: 100%).

(2) Cross-sectional areas also perpendicular to the tensile test direction but situated at locations other than the grid nodes. The proportion of solid material in these areas is detailed in Tables 1 and 2.

The parameter P_s pertains to the second type of cross-sectional area, as this type is considerably more important. Most potential relevant cross-sectional areas in the grids fall into this second category. This consideration assumes that the thin walls orthogonal to the tensile testing direction have a relatively low impact on the macroscopic mechanical response of the structure in the tensile tests.

2.2 Metal powder

Two plasma atomized powders were employed: AlSi7Mg0.6 powder and IN718 powder with a particle size distribution of 20–63 µm and 15–45 µm, respectively. The chemical composition of these powders was analyzed by Inductively Coupled Plasma (ICP) spectroscopy and is given in Table 3. Both powders showed very spherical morphology, with a presence of a few satellites, low internal porosity, and a continuous flow (Fig. 2, top left and bottom left). The particle size distribution showed a cumulative 50% in volume (D50) of 49 µm and 34 µm for AlSi7Mg0.6 and IN718 powder, respectively. Moreover, the internal porosity of the employed powders was analyzed by preparing metallographic samples and performing an optical analysis (Fig. 2, top right and bottom right). The AlSi7Mg0.6 and IN718 powders had an internal porosity of 0.33 ± 0.16% and 0.10 ± 0.06%, respectively, as measured by optical microscope (Olympus GX51) and using analySIS docu image analysis software.

Table 4 PBF-LB/M processing parameters used for AlSi7Mg0.6 and IN718

Material	PBF-LB/M processing parameters		
	Layer thickness (µm)	Power (W)	Speed (mm/s)
AlSi7Mg0.6	30	150–325	500–1200
IN718	60	150–200	700–1000

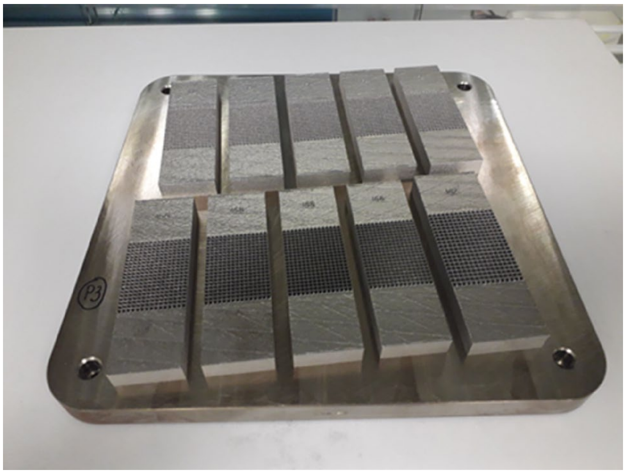

Fig. 3 Samples on their building platform after the fabrication via PBF-LB/M in IN718 material

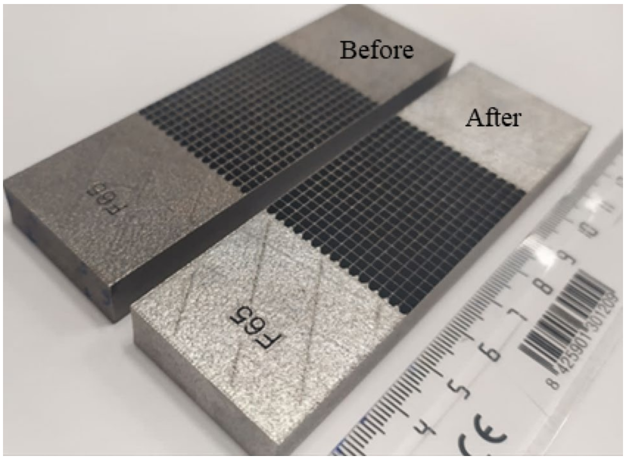

Fig. 4 Exemplary AlSi7Mg0.6 samples after removal from the building platform before and after chemical treatment

2.3 Sample manufacturing

Samples were built on a SLM Solutions machine model SLM 280HL. It is equipped with a 400 W fiber laser (Yb fiber, λ: 1050 nm) which has a Gaussian shape and a spot size in the range of 80–120 µm according to machine manufacturer and operates under a protective Argon atmosphere, guaranteeing a maximum allowed oxygen content of 0.2% during manufacturing. The processing parameters for each material are summarized in Table 4. The parameters were varied to achieve different wall thicknesses in the grid area.

Table 5 Heat treatments applied to samples manufactured from AlSi7Mg0.6 and IN718

Material	Heat treatment	Atmosphere
AlSi7Mg0.6	Ageing 160 °C, 6 h	Air
IN718	Solution annealing at 1037–1065 °C + double ageing step 760 °C + 650 °C	Argon

Samples were manufactured directly on a platform, without using supports, with an additional extrusion of the geometry of 1 mm at their base to allow for easy separation of the samples from the platform using wire cutting. During the wire-cutting process the additional 1 mm of material were removed. Figure 3 shows an exemplary building platform with samples processed in IN718 material. This manufacturing was carried out applying the above describe processing parameters (see Table 4). A visual inspection was performed after wire-cutting and prior to subject of samples to a surface treatment (Fig. 4). No cracks were detected in any sample.

2.4 Heat treatments

Both materials were subjected to specific heat treatments to improve their mechanical properties. Samples were heat treated attached to the baseplate to reduce the thermal stress and prevent distortions during removal from the platform. The applied heat treatments promote the precipitation of hardening particles, namely γ'-Ni_3(Ti, Al) and γ'-Ni_3Nb precipitates in IN718 material and Mg_2Si precipitates in AlSi7Mg0.6 material. The fine and uniform distribution of these precipitates throughout the matrix allows an increase in the hardness and ductility of the samples. Table 5 shows the applied heat treatment conditions for each material. The microstructures of PBF-LB/M parts differ from those of conventionally produced parts. The heat treatments applied in this work are tailored to the parts manufactured by PBF-LB/M. The heat treatments, therefore, can differ from commonly used heat treatments for these materials conventionally processed. IN718 samples were subjected firstly to a homogenization treatment to homogenize the microstructure and dissolve the γ' and γ'' phases on the matrix and then an ageing heat treatment was applied to promote the precipitation of the same phases but with very small size and uniformly distributed throughout the matrix based on a previous study [54]. In the case of AlSi7Mg0.6 only an aging heat treatment was applied since previous works [55] demonstrated the effectiveness of eliminating the previous steps (solution treatment followed by quenching) related to conventional heat treatments such as T6 [56].

2.5 Surface treatments

As surface roughness was found to be a key parameter to consider regarding the thermal and hydraulic characteristics of additively manufactured metal heat exchangers [6], surface treatments were considered in this work. Chemical polishing was identified as the best surface treatment to reduce the roughness of internal channels in the grid structures. The selection of the electrolytes and process parameters, mainly electrolyte temperature and movement, polishing time and surface pre-treatment, were selected considering CIDETEC's experience.

Figure 5 shows the surface treatment for AlSi7Mg0.6 samples and IN718 samples. AlSi7Mg0.6 samples were surface-treated using an electrolyte based on 85% of H_3PO_4 at 80 °C for 20 min. After polishing, the samples were rinsed with water. IN718 samples were surface treated using an acid mixture based on $HCl+HNO_3$ at 40–45 °C for 15 min. Before chemical polishing, IN718 samples were pretreated in order to remove the oxide layer produced on the surface of these samples during the heat treatment. The pre-treatment process consisted of immersing the samples in an electrolyte solution containing NH_4HF_2 and HNO_3 at room temperature for 7 min, followed by neutralization in 40% NaOH at 45 °C for 3 min. After the chemical polishing step, the same NH_4HF_2–HNO_3 electrolyte was used to remove the oxides formed during the process; this rinsing step lasted 1 min. The image of samples before and after the surface treatment can be seen in Fig. 4. Both, AlSi7Mg0.6 and IN718 samples were surface treated by immersing the parts in the electrolytes.

2.6 Surface roughness analysis

Surface roughness was measured inside the channels using a Taylor–Hobson Talysurf-Intra-50 mm profilometer after AlSi7Mg0.6 and IN718 samples were tested. In the case of AlSi7Mg0.6 samples the roughness was also measured on the bulk material part of the specimens. The roughness was calculated using the average Ra values. The morphological characterization of the surfaces was carried out with a JEOL JSM-5500LV Scanning Electron Microscope (SEM).

2.7 Density analysis and microstructure analysis

Density analysis of the samples was performed analogously to the case of the metal powder. Again, metallographic samples were prepared and an optical analysis was performed by optical microscope (Olympus GX51) and using AnalySIS docu image analysis software.

Furthermore, samples to be characterized in terms of microstructure were sectioned, mounted in epoxy material, ground, polished, etched and subsequently examined using a Zeiss Ultra Plus Field Emission Scanning Electron Microscope (FE-SEM).

2.8 Fracture surface analysis

Fracture surfaces of the tensile specimens were also analyzed using a Zeiss Ultra Plus FE-SEM.

2.9 Tensile testing

In this section, information about the preparation of samples for the Digital Image Correlation (DIC), the experimental

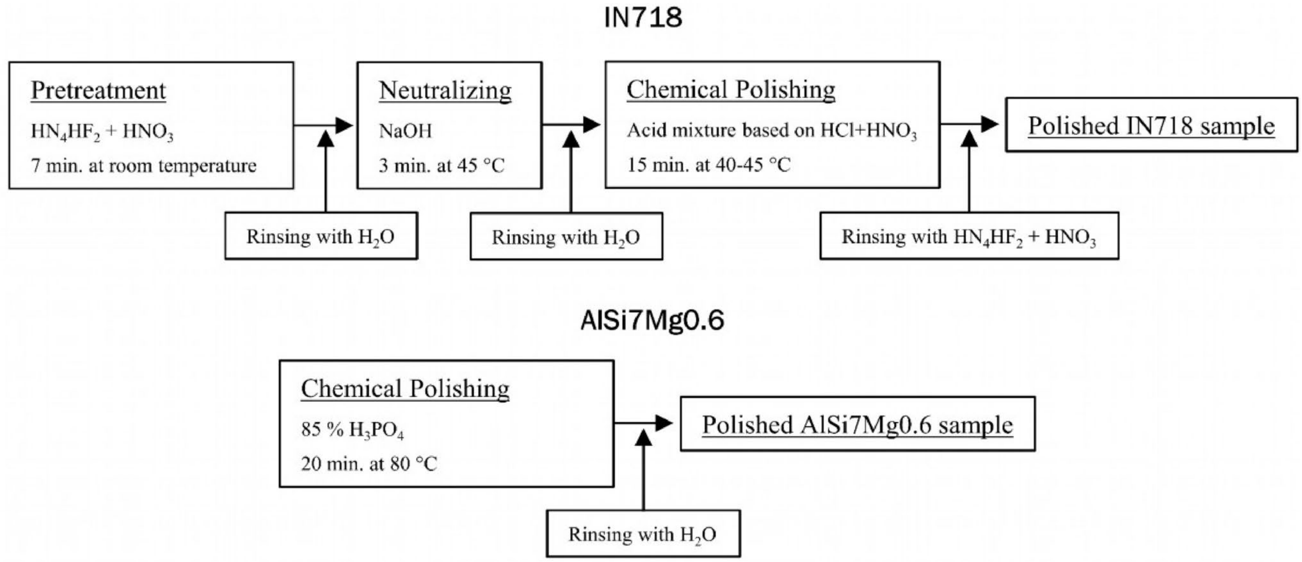

Fig. 5 Surface treatment sequence applied to reduce the surface roughness of IN718 and AlSi7Mg0.6 samples

setup, conduct of tests and data evaluation methods are presented.

2.9.1 Sample preparation

Manufactured samples were painted with a speckle pattern in the areas of interest to enable the evaluation of DIC data, which includes automatic recognition of points on the sample surface at all time steps.

2.9.2 Experimental setup

Figure 6 shows the experimental setup with which the tensile tests with simultaneous recording of DIC data were conducted. A Zwick tensile testing machine with a maximum force of 100 kN was used. Pre-tensioned wedge-clamping jaws were used during the experiments. The tensile testing machine was controlled using a computer. This computer recorded force data as well as the crosshead displacement.

The DIC system consisted of two cameras, a lighting system and an additional computer. A 100 mm Aramis 4 m system with a measuring volume of $65 \times 48\ \mathrm{mm}^2$ was used. The calibration object that was used was CQ/CP20 $55 \times 44\ \mathrm{mm}^2$. The computer connected to the DIC system recorded force data directly from the tensile testing machine as well as the footage recorded by the cameras.

2.9.3 Testing

The strain rate was chosen conservatively to ensure high-quality results. The chosen strain rate for all samples was $7 \times 10^{-5}\ \mathrm{s}^{-1}$ with respect to the measuring lengths m of the samples (see Fig. 1 and Appendix Table 10) based on DIN EN ISO 6892 [57]. The temperature in the laboratory was in a range between 20 and 23 °C for all tensile tests. The distance between clamps was adjusted for each sample type according to its measuring length. Both cameras of the DIC system recorded at 1 Hz. This sampling frequency was selected based on the expected strain rates and deformation speeds, aiming to capture the strain evolution accurately while avoiding excessive data volume.

2.9.4 Data collection

Data was collected by combining information from the DIC system and the tensile testing machine. Equivalent tensile stresses were calculated by dividing the occurring absolute force by the A_T of the respective sample.

2.9.5 Strain measurement

Strains were evaluated from the DIC footage. The software GOM Correlate 2020 was used for this task. Figure 7 shows so called “facet points” that were used to measure strains in the DIC footage. The facet points were placed in the same columns of nodes of the grid structure in one of the two center columns of the grid. The lower facet points were located in the last row of the grid. For some samples, the top facet points were located in the second row of the grid to ensure that the points were always within the field of view of the DIC system. For some samples facet points were located in transition areas (close to radii at interface between grid and bulk material), as this was necessary to obtain meaningful strain measurements depending on the break location. Automatic recognition of the points was used to identify the points in all time steps. In the next step automatic recognition was reviewed and corrected if necessary.

Fig. 6 Photographs of experimental setup for tensile testing with additional Digital Image Correlation system (DIC) with overall setup (left), detailed photograph of camera location (top right) and detailed photograph of a sample in the test setup (bottom right)

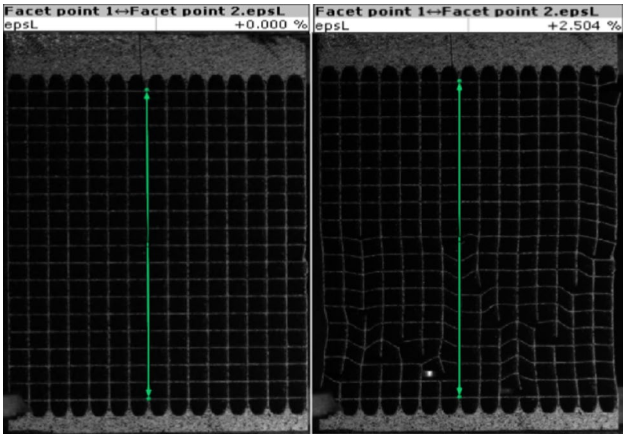

Fig. 7 Screenshots illustrating the evaluation of strain values for a representative sample based on DIC data. The change in distance between the highlighted points, labeled as 'epsL' in the software, corresponds to the strain calculated relative to its load-free state at the beginning of the measurement

2.9.6 Data post-processing

A smoothing of the stress–strain curve was conducted to account for noise in force measurement and strain measurements by DIC. From the stress–strain curve, only the information up to the first local rupture was considered to determine the equivalent mechanical properties of thin-walled grid type structures. First, the curve was divided into its linear part (elastic deformation) and, if present, into its nonlinear part (plastic deformation). From the linear part the Equivalent Young's Modulus (EYM) was identified by means of a linear regression based on the standard DIN EN ISO 6892-1 [57]. In the case that no plastic deformation was present, the maximum elastic stress and strain were also designated as the ultimate ones. On the contrary, in case the plastic deformation indeed was present, the equivalent elastic limit was defined following the 0.2% offset yield strength method. The maximum load reached after the plastic deformation was used to define the Equivalent Ultimate Tensile Strength (EUTS).

In addition, the uncertainties related to the load measurements of the tensile testing machine and to the deformation measurement of the DIC system, together with the uncertainties related to the caliper used for measuring the thickness of the walls and the width and depth of the samples, were considered to evaluate the overall uncertainty δ, given by,

$$\delta^2 = \sum_{i=1}^{i=N} \left(\frac{\partial \phi}{\partial x_i} \delta_{x_i} \right)^2 \tag{1}$$

where ϕ is the measured magnitude depending on N magnitudes represented by x, each of those x_i owning a particular uncertainty interval δ_{x_i}. From the above, the wall thickness measurement was the most influential one as it directly affects the proportion evaluation. However, it is not such a relevant parameter for calculating the equivalent properties, although it would be relevant for determining the local stress supported by the walls.

These uncertainties are reflected in the figures in the results section. The horizontal error bars are related to the uncertainty of the thickness measurement. The vertical error bars, on the other hand, reflect the maximum positive and negative deviation from the mean value shown by the three samples of the same reference. These values in turn include the overall uncertainty δ.

Table 6 Literature values of Young's moduli and ultimate tensile strength of AlSi7Mg0.6 and IN718 manufactured via PBF-LB/M for bulk materials, and chosen parameters of the FEA non-linear material models

	AlSi7Mg0.6	IN718
Literature values		
Young's modulus [GPa]	63 [55]	191 [58]
Ultimate tensile strength [MPa]	444 [55]	1406 [58]
FEA Material Model		
Young's modulus [GPa]	63	191
Initial yield stress σ_0 [MPa]	282	1211
Steady-state flow stress σ_s [MPa]	453.7	1431
Saturation coefficient m	48.24	64.83
Saturation exponent n	0.9849	0.9738

2.10 Reference models based on bulk materials

For comparison of results from experiments and Finite Element Analysis (FEA) to information from literature, literature data on tensile tests using dog bone test samples was used. For relevant data on material properties of AlSi7Mg0.6 and IN718 processed by PBF-LB/M data from [55] and [58] were used, respectively (see Table 6). In both studies the data is based on tensile tests with dog bone samples.

The Young's modulus greatly depends on the cross-sectional area and is often identified using dog bone test samples that consist of bulk material. Solid material (without voids) is assumed for the respective cross-sectional area of interest. EYM is approximated by multiplication of the Young's modulus with the proportion of solid material in majorities of cross-sectional areas (P_s) of the respective sample (see "Reference" in Fig. 17).

2.11 Finite element analysis

In this section, set-up of the FEA, evaluation methods of equivalent stresses and equivalent strains in the FEAs and the meshing are presented. FEA was performed in COMSOL Multiphysics 5.2a [59].

2.11.1 Non-linear material models

In order to accurately simulate the mechanical behavior of AlSi7Mg0.6 and IN718 under various conditions, non-linear material models were developed for the FEA. The non-linear material models were developed based on experimental data on bulk material tensile test samples in the articles [55] and [58] for AlSi7Mg0.6 and IN718, respectively. Heat treatments in these studies were sufficiently similar to those that were used in the work at hand. The derived Young's moduli were used for simulation of the elastic deformation of the materials. For simulation of plastic deformations, Hockett–Sherby strain hardening [60] as implemented in COMSOL Multiphysics 5.2a [61] was utilized. The governing equation for the stress σ at a given effective plastic strain ε is

$$\sigma = \sigma_0 + (\sigma_s - \sigma_0)(1 - e^{-m\varepsilon^n}) \tag{2}$$

with the initial yield stress σ_0, the steady-state flow stress σ_s, the effective plastic strain ε, the saturation coefficient m, and the saturation exponent n. The respective material parameters used for both material models can be found in Table 6.

2.11.2 Boundary conditions and study type

Figure 8 shows an exemplary model of the FEA. Two planes of symmetry (parallel to x–y-plane and parallel to x–z-plane) were used for all models reducing the number of finite elements, thereby decreasing computing costs. Furthermore, mechanical boundary conditions were introduced in the clamping areas of the samples. A domain of 15 mm length was mechanically fixed at one end of the sample and another domain of 15 mm length was subjected to a prescribed displacement at the other end of the sample (see Fig. 8). The prescribed displacement was defined as parallel to the x-axis, such that the structure was put under tension.

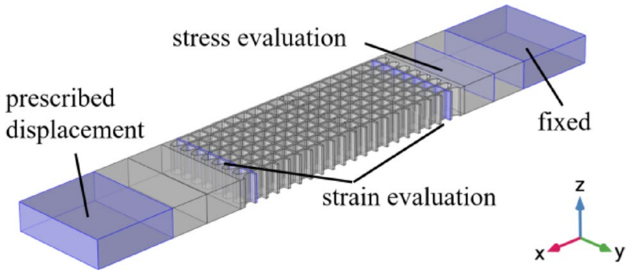

Fig. 8 Screenshot of a representative finite element analysis model of a sample showing areas of interest: the mechanically fixed volume, the volume subjected to a prescribed displacement, the plane where stresses are evaluated, and the two planes where strains are evaluated

A series of stationary studies with prescribed displacements was run for each sample to numerically investigate the tensile tests. Besides using non-linear material models as presented previously, geometric non-linearity was considered in the simulations. No failure model was implemented.

2.11.3 Evaluation of equivalent stresses and equivalent strains

Due to Newton's first law of motion (equivalent) stresses of cross sections along the x-axis could be expected to be equal for the model. As stress peaks in the thin-walled structure were expected to be unfavorable in terms of numerical inaccuracies in evaluation of the equivalent stresses, the equivalent stress was measured in one cross-sectional boundary between the fixed domain and the thin-walled structure as shown in Fig. 8. The average von Mises stress was evaluated for all FEA sample types at this boundary.

The strains were measured based on the average displacements in x-direction of two boundaries for each sample type according to Eq. (3). The respective boundaries are highlighted in Fig. 8.

The average strains ε_{av} were calculated based on the initial average x-coordinates $x_{1,init,av}$, $x_{2,init,av}$ of boundaries 1 and 2, respectively. Furthermore, the average strains ε_{av} were calculated based on the stationary results for the average x-coordinates $x_{1,fin,av}$ and $x_{1,fin,av}$ of boundaries 1 and 2, respectively, according to

$$\begin{aligned}\varepsilon_{av} &= \frac{\Delta x_{2,av} - \Delta x_{1,av}}{\Delta x_{init,av}} \\ &= \frac{(x_{2,fin,av} - x_{2,init,av}) - (x_{1,fin,av} - x_{1,init,av})}{(x_{2,init,av} - x_{1,init,av})}.\end{aligned} \tag{3}$$

2.11.4 Evaluation of EYM, EYS and EUTS from FEA

EYM of the FEA was evaluated using the same criterions as were described in the previous section on experimental tensile testing. The evaluation of the EYS was conducted by determining the moment at which the von Mises stress first exceeded the yield strength of the material within one of the critical cross sections of the specimen. Analogously, the EUTS was evaluated by identifying the instant at which the von Mises stress exceeded the value of the Ultimate Tensile Strength (UTS) of the material for the first time in one of the critical cross-sections of the sample.

2.11.5 Discretization of geometry

The meshes of all numerically investigated sample types were set up similarly to ensure comparability. For all sample types, the grid was discretized using brick elements, which are three-dimensional hexahedral finite elements. The size of the brick elements was chosen to be approximately half of the wall thickness of the corresponding samples, ensuring adequate resolution of results. Therefore, the thin walls were discretized by two layers of finite elements. Outside the grid area, a transition from brick to tetrahedral elements was applied, enabling an automatic meshing algorithm for the remaining areas. In these areas, larger elements were used because high deformations and stresses were not anticipated, allowing these larger elements to still yield high-quality results. Each element's displacement field was modeled using quadratic serendipity to maintain high-quality outcomes.

A mesh convergence analysis was conducted to ensure that discretization by two layers of finite elements gives results of high quality. Representative samples with a wall thickness of 0.3 mm were chosen for this part of the study. Three FEAs were set up and evaluated. Within the three FEA models, thin walls were discretized by one, two, and three finite-element layers, respectively. Equivalent stress–strain curves were derived from the data. Curves for two and three finite element layers demonstrated good agreement, while the curve for one finite element layer did not accurately represent the high strain region. Root Mean Squared Errors (RMSE) for the models with one and two finite element layers were calculated. The stress–strain curve of the model with three finite element layers was considered a reference. High strains, for which the model with one finite element layer performed poorly, were excluded. The model with two finite element layers had a RMSE of 0.080 MPa, while the model with one finite element layer had a RMSE of 0.246 MPa with the maximum occurring equivalent stresses in all three models being close to 60 MPa. It is noted that the model with two finite element layers had a better RMSE value even though high strains, in which the model with one finite element layer gave poor results, were excluded from RMSE evaluation. Consequently, it was concluded that using two element layers for discretization along the thickness of the thin walls provides accurate results also for the other sample types investigated in this work.

3 Results and discussions

This section presents and discusses the results of density analysis, microstructure analysis, surface roughness analysis, FEA and tensile testing experiments.

3.1 Density analysis and microstructure analysis

The relative density varied from 97.75 to 99.38% for AlSi7Mg0.6 and from 99.73 to 99.97% for IN718. These density variations are due to the different process parameters applied during additive manufacturing. The processing parameters were varied and optimized to achieve different wall thicknesses. As an example, the optical micrographs of grid-like structures are shown for both materials (Fig. 9). Samples made of AlSi7Mg0.6 material showed more and larger pores than those of IN718 regardless of their processing parameters due to the material properties. AlSi7Mg0.6 grid-like structure showed pores on the thin wall areas and on the intersection areas. The melt pools and heat management are different on those areas and, consequently, the observed pores differ in their size and origin. Pores at intersection areas are larger than those of thin walls and they are called open pores. Some studies [29, 62] conclude that these pores on grid-like structures are formed since the molten liquid cannot fill the voids between powders while the small pores, namely, the metallurgical pores arose from the gas entrapped in the molten pool. On AlSi7Mg0.6 sample the open pores have a size from 40 to 60 µm, while the pores of thin walls vary from less than 2–30 µm. In the case of IN718 sample, there is no open pores and the metallurgical pores varies from less than 1–20 µm.

A heat-treated AlSi7Mg0.6 tensile sample was analyzed by FE-SEM microscope on the XY plane to study its microstructure. The micrographs show a cellular-dendritic solidification structure with α-Al matrix (grey) and eutectic Si-rich phase (white) located mainly along cells but also inside these cells (Fig. 10). The Si-rich particles detected inside cells present sizes around 30–230 nm. (Fig. 10c, d). Some pores are detected (Fig. 10a) since the processing parameters were optimized for achieving lower wall thicknesses and not for achieving the highest densities. The Mg_2Si precipitated during ageing were not detected by FE-SEM due to their low size. TEM analysis will be required to detect them. These observations are in line with the findings of other authors [55, 63].

The microstructure of a heat-treated IN718 tensile sample without surface treatment was studied on XY plane by FE-SEM. The microstructure showed an FCC γ-nickel matrix with columnar grains (Fig. 11a, b). δ- phases with a rod-short shape together with metal carbide precipitates (metal probably Ti or Nb) were detected located mainly on the grain boundaries and some of them also inside grains (Fig. 10c–f). These phases, which are detrimental for the mechanical properties, are also observed in other IN718 samples processed by PBF-LB/M after homogenization, solution and double ageing heat treatments [64] and after solution heat treatment at 980 °C followed by double ageing steps at 720 and 650 °C [65]. Laves phases are not identified after performing compositional analysis of the precipitates since there was a lack of Mo on them.

Fig. 9 Optical micrographs showing pore size and location of AlSi7Mg0.6 (left) and IN718 (right) grid-like structures

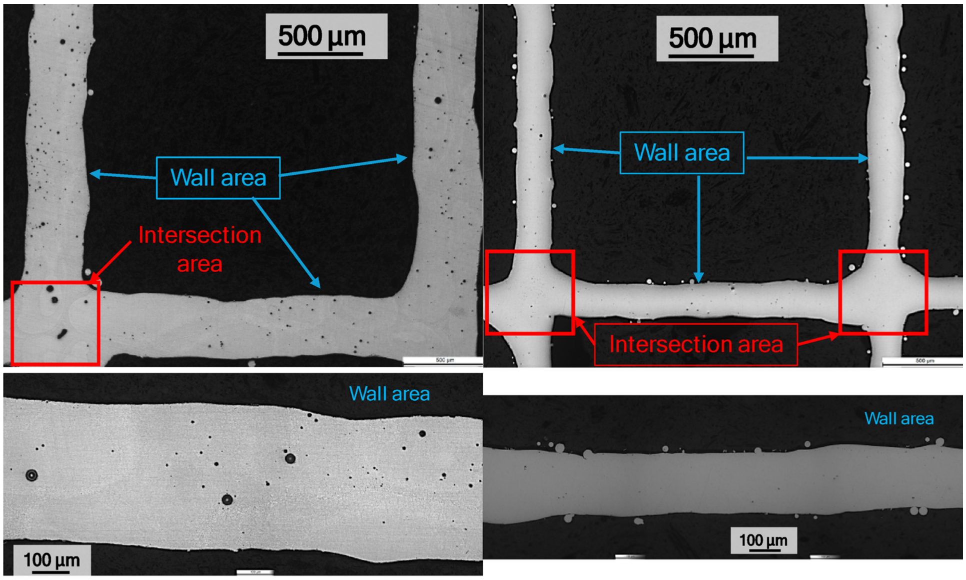

A7_nST sample; density: 98.42 %; Average wall thickness: 0.353 mm

I6_nST sample; density: 99.73 %, Average wall thickness: 0.171 mm

Fig. 10 Microstructure of AlSi7Mg0.6 tensile sample after direct ageing heat treatment

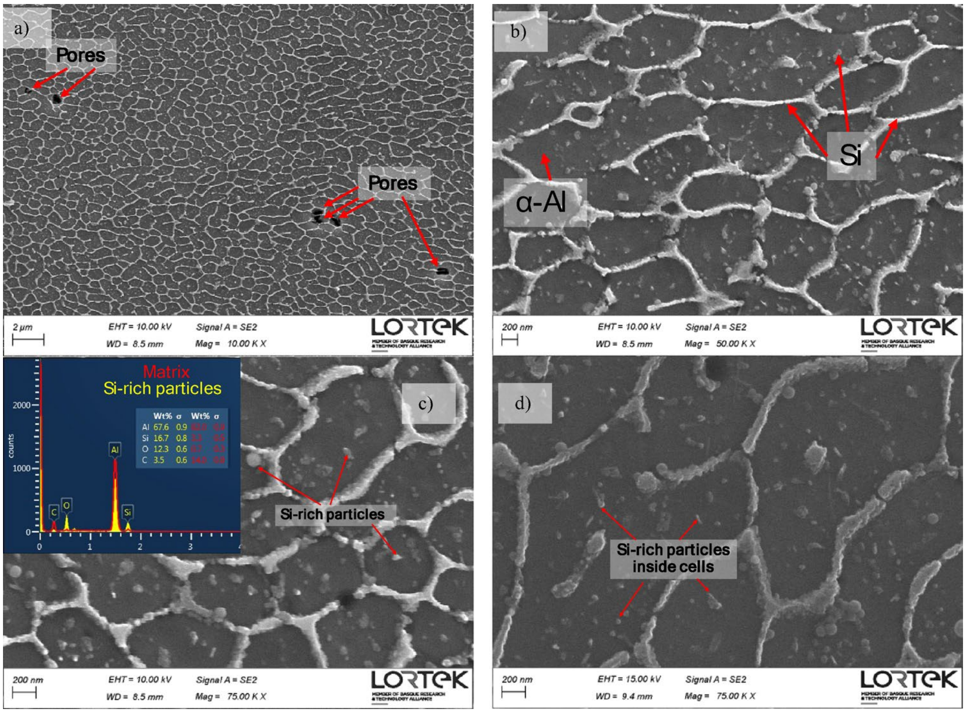

3.2 Surface roughness analysis

Surface roughness was measured inside channels for surface-treated samples and, additionally, for some non-surface-treated samples after tensile testing. Table 7 details the Ra values before and after surface treatment for AlSi7Mg0.6 and IN718 samples. The chemical treatment reduced the roughness of all types of the measured samples. Comparing AlSi7Mg0.6 samples, A7 samples showed the smallest reduction of the Ra of 5.32% while A4 showed the greatest reduction of the Ra of 27.88%. In the case of IN718 samples, I6 samples showed the smallest reduction of the Ra of 20.88% while I8 samples showed the greatest reduction of the Ra of 41.08%.

The SEM analysis of the surface morphology before and after surface treatment revealed that the chemical treatment was able to successfully remove all the partially melted metallic particles as can be seen in Fig. 12. Reduction of the Ra value in combination with the removal of the partially melted particles is important for the application of

Fig. 11 Microstructure of heat-treated IN718 tensile sample showing precipitates. Energy Dispersive X-Ray Spectroscopy (EDS) spectrum analysis diagram of the precipitates is shown

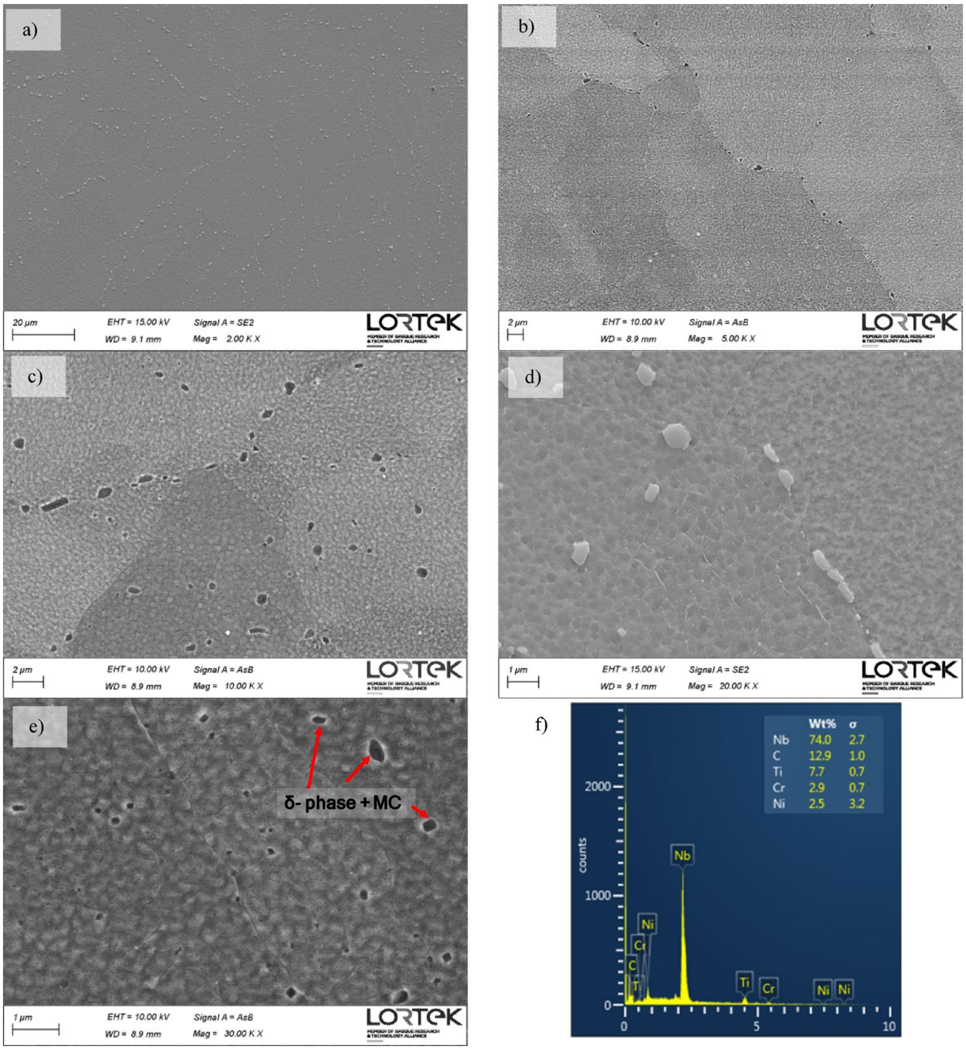

Table 7 Surface roughness (Ra) of non-surface-treated and surface-treated AlSi7Mg0.6 and IN718 samples

	Roughness, Ra (µm)	
	Non-surface-treated	Surface-treated
AlSi7Mg0.6 samples		
A1	8.53 ± 1.54	6.92 ± 0.41
A2	11.98 ± 2.87	9.14 ± 0.36
A3	–	10.79 ± 3.12
A4	8.86 ± 1.10	6.39 ± 0.77
A5	–	11.76 ± 2.45
A6	–	9.84 ± 1.79
A7	8.46 ± 1.19	8.01 ± 1.14
A8	–	10.23 ± 1.13
IN718 samples		
I1	10.31 ± 1.01	7.04 ± 1.03
I2	–	9.14 ± 0.79
I3	–	6.83 ± 0.33
I4	9.27 ± 0.89	7.02 ± 1.59
I5	–	7.93 ± 0.91
I6	8.19 ± 0.55	6.48 ± 1.41
I7	–	7.23 ± 1.16
I8	10.32 ± 1.87	6.08 ± 0.74

thin-walled structures in heat exchangers to achieve small pressure losses. This is connected to the fact that one important design constraint of heat exchangers in aviation applications is a low drag especially on the air side.

3.3 Finite element analysis

FEA showed that highest stresses occurred in the grid structure for all sample types, whereas rather low stresses occurred at the clamping areas, as anticipated. Therefore, the simulations suggest rupture of the samples in the grid structure.

Relationships between equivalent stress and strain for the six different simulated grid structures could be derived from the FEA. Furthermore, for all samples an EYM, EYS and an EUTS could be deduced from the simulation results. The results of the numerical analysis are presented alongside the results of the experimental analysis in the following subsection. A limitation of the FEA is that perfect geometric accuracy based on the CAD-files is considered, while the

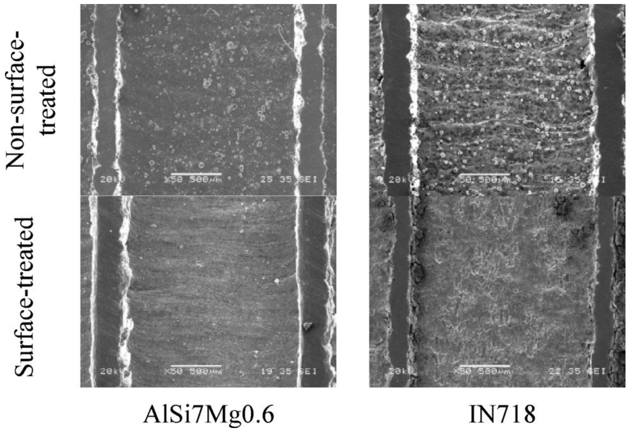

Fig. 12 Surface micrographs obtained by SEM in internal channels of AlSi7Mg0.6 and IN718 samples before and after the surface treatment

additively manufactured samples have geometric irregularities such as a certain variation in the actual wall thicknesses in each sample. Furthermore, the used material models are based on bulk material experiments. As a result, the effect of internal defects, surface roughness, and the microstructure, which is considered indirectly by the material model, could be over- or underestimated in the FEA. This is because the effects of these aspects may differ in thin-walled structures compared to bulk materials. Another natural limitation of the FEA is given by the mesh refinement and the resulting accuracy of the computed solution. However, the mesh convergence analysis showed that mesh convergence was achieved meaning that the errors induced by this aspect could be reduced sufficiently.

3.4 Tensile testing

In this section, results of experimental tensile tests are presented and compared to results from simulations based on properties reported in the literature. First, the influence of wall thickness on the morphology of stress–strain curves and the failure mode are discussed. Finally, the results regarding EYM, EYS and EUTS of the different samples are presented. During the evaluation phase, a representative subset of 60 experimental samples were considered. A total of 12 samples were not included in the final evaluation for the following reasons: Five samples were damaged during machining. One sample was tested at an incorrect traverse speed. Five evaluation files were corrupted and could not be recovered. One sample's file was considered an outlier and was removed from the data.

3.4.1 Morphology of stress–strain curves and failure mode

It is important to show the differences in the tensile behavior exhibited by samples of different thicknesses. As an example, Fig. 13 shows three characteristic stress–strain curves measured on AlSi7Mg0.6 samples whose wall thicknesses (t) and proportions (P_s) are in the low, medium, and high range of the wall thicknesses analyzed in this study.

The criterion established to determine the mechanical properties was to consider the stress–strain data up to the first breakage. Thus, in Fig. 13a–c, the thicker gray curve represents the entire test history up to the total failure of the sample, whereas the thin black line represents the curve measured up to the first breakage, that was used for the data evaluation that is presented in the upcoming sub-sections. As can be seen in Fig. 13a, the thinner specimens showed poor mechanical behavior, with only elastic deformation before the first local rupture of one of the vertical walls which was manifested by a sudden drop in the force signal. Continuing the test, the value of the force increased again until another sharp drop was measured, indicating another local breakage of some other vertical wall. The process continued even exceeding the maximum stress acquired at the initial breakage. Similarly, the regions of load restitution became less pronounced, indicating that the structural deformation was no longer due to elongation of the vertical walls but rather the bending deformation of the horizontal walls, which continued to hold the already damaged parts together (see sequence shown in Fig. 13a). The breakage pattern was random between specimens of the same thickness and may be caused by an arbitrary distribution of defects. It is noted that defects are a common problem in PBF-LB/M including the processing of AlSi7Mg0.6 [25] and IN718 [26]. Due to the low thickness of the walls, the relative influence of defects that produce a reduction of the effective cross-sectional area is larger as the thickness is reduced. This, combined with the associated stress concentration, leads to rupture before a noticeable plastic deformation of the structure becomes apparent. As the thickness increased, this arbitrary fracture pattern was reduced achieving expected stress–strain curves with elastic and plastic regions as can be seen in Fig. 13b, c. In these cases, defects did not appear to have such a decisive effect in terms of causing the initiation of breakage in several arbitrarily distributed regions. However, they were certainly contributing to the reduction of the load-bearing section and increasing stress concentration, causing the structure to show evident plastic deformations, even before reaching the expected elastic limit that the numerical results suggested shown by a vertical dashed line in Fig. 13.

The surface of tensile fracture of a A7_ST AlSi7Mg0.6 (t=0.225; P_s=0.1035) sample, which is in the upper range of the thickness, was analyzed by FE-SEM to correlate the failure mode with presented defects on the microstructure. The structural deformation on this specimen was due to the bending deformation of the horizontal walls (Fig. 14a). The first grid broken (Fig. 14a, blue square) was analyzed but

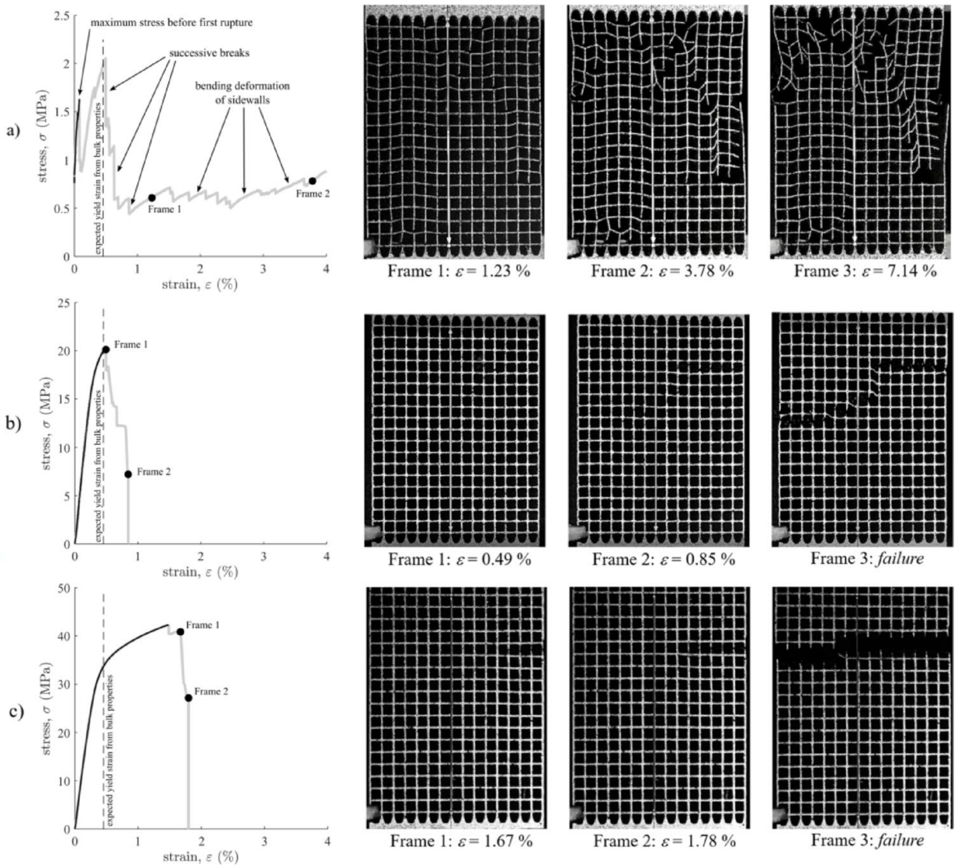

Fig. 13 Tensile stress–strain curves of AlSi7Mg0.6 samples with different wall thicknesses (t) and solid material proportions (P_s). Black lines indicate data up to the first local rupture; gray lines show full test duration. Panels correspond to: **a** $t = 0.089$ mm, $P_s = 0.0468$ (low thickness); **b** $t = 0.136$ mm, $P_s = 0.0625$ (medium thickness); and **c** $t = 0.225$ mm, $P_s = 0.1034$ (high thickness). Selected Digital Image Correlation (DIC) frames visualize deformation stages

the crack initiation cannot be detected since the fracture surface was very complex. This surface combined areas with a brittle and ductile fracture (Fig. 14b). Some specific cracking propagation paths were observed which are perpendicular to the applied load (Fig. 14c). The metallurgical pores were also detected on the fracture surface (Fig. 14c), but they were not responsible for the crack beginning and propagation. Microvoids are observed on the ductile fracture surface (Fig. 14d). A dimple-like feature was observed which could correspond to a debonding of a Si-rich cell or Si precipitates (Fig. 14e) since the size of the dimple did not correspond with the Si-rich particles located inside cells (Fig. 10c, d). This is coherent with some authors [66] who detected Si precipitates on AlSi10Mg fracture surface cavities, of a sample processed by PBF-LB/M, which were a preferred path for crack propagation. Other authors [67], who analyzed the fracture surface of a PBF-LB/M processed AlSi10Mg alloy, conclude that the plastic deformation led to a debonding of Si-rich cell interface of the α-Al matrix provoking dimples on the fracture surface. Micrographs at higher magnifications show pores and microvoids typical of a ductile fracture surface.

Figure 15 shows representative stress–strain curves of IN718 samples, generated analogously to those of the AlSi7Mg0.6 specimens. Again, the stress–strain curve together with the test sequence is shown for the lower, middle and upper range wall thickness values.

As with AlSi7Mg0.6 samples, similar fracture modes were identified as the thickness increased. The thinnest specimens showed random failure initiation with consecutive ruptures of the vertical walls (vertical stress drops), followed by the progressive restitution of the load value indicating the bending deformation of the horizontal walls. Once again, no clear breakage pattern was observed in the specimens with lower wall thickness. Conversely, as the thickness increased, the rupture pattern became more localized, with rupture manifesting itself in vertical walls located at the same height, or at several neighboring heights. Finally, the thicker samples showed a remarkable plastic deformation up to the almost simultaneous rupture of all the walls in both materials.

Further on in the analysis, the fracture mode is related to the proportion showing that each material presents a different threshold which must be exceeded to guarantee a plastic deformation before rupture occurs. The applied surface treatment did not have any additional noticeable effect on the fracture mode apart from its direct influence on wall

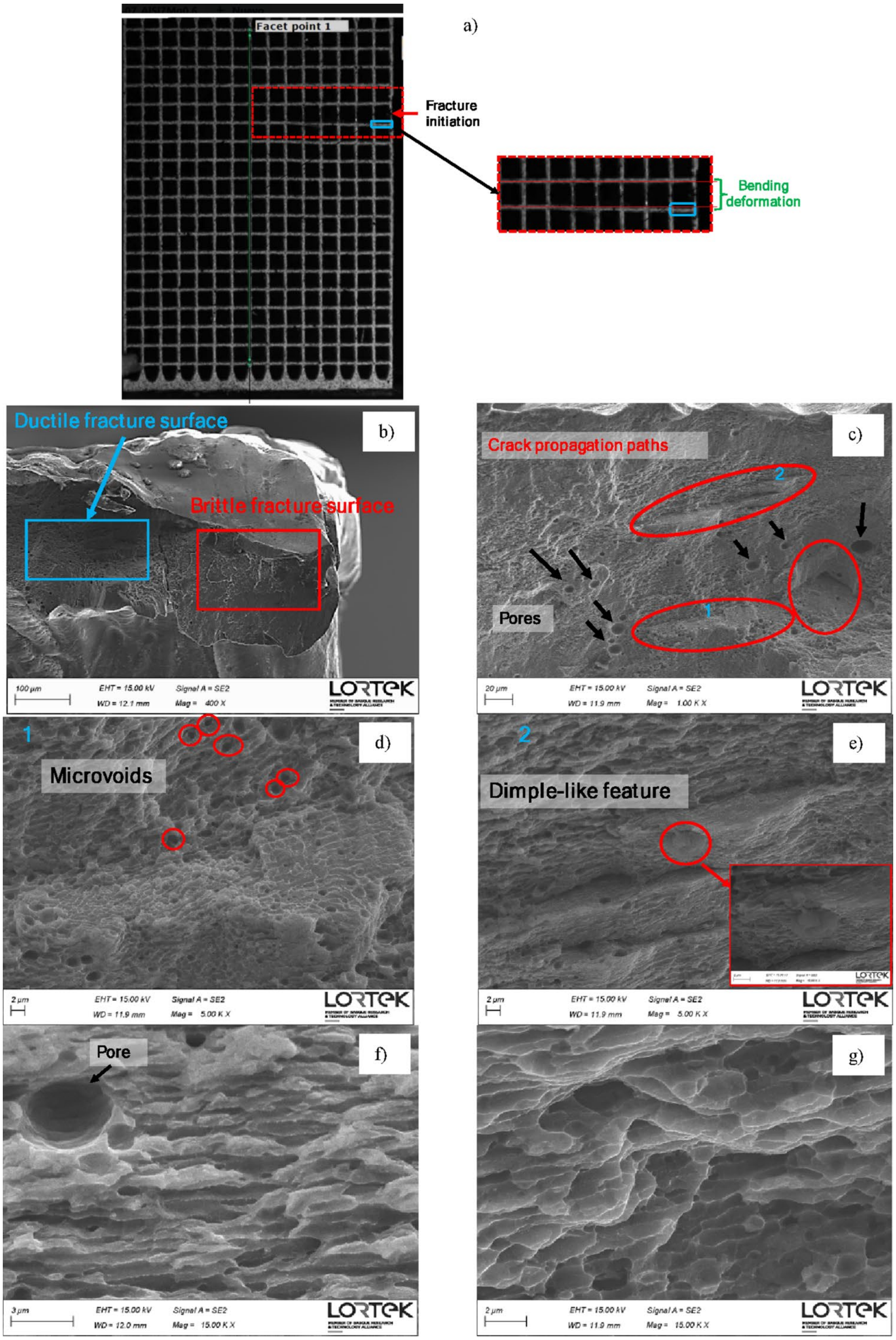

Fig. 14 Fracture surface analysis of an AlSi7Mg0.6 tensile specimen with wall thickness $t=0.225$ mm and solid material proportion $P_s=0.1035$ after tensile failure. **a** Image of highlighting the grid of the fracture initiation (red arrow) and the area of the bending deformation of the horizontal wall. The blue square highlights the fracture surface analyzed by a Field Emission Scanning Electron Microscope (FE-SEM). **b** Micrographs showing an area with a ductile and brittle fracture surfaces; **c** crack propagation paths and pores; **d** magnification of the site 1, of micrographs from c), showing microvoids; **e** magnification of site 2, of micrographs from c), showing dimple-like feature. Micrographs at higher magnification showing pores in **f** and microvoids in **g** on a ductile surface fracture area

thicknesses and P_s values, which directly affect the macroscopic mechanical responses of the structures.

The surface of tensile fracture of a I6_nST IN718 sample ($t=0.170$; $P_s=0.0869$), which is in the upper range of the thickness for this material (Fig. 15c), was analyzed by FE-SEM microscopy. All the walls were broken almost simultaneously. The first grid of the horizontal wall was analyzed (Fig. 15c, red arrow). An irregular fracture surface with different height levels was observed through the grid (Fig. 16a, b). Powder particles attached to the surface of the vertical wall of the grid were observed as this sample was not surface treated. Fracture surface combined ductile and brittle fracture areas. Ductile fracture surfaces showed microvoids and dimples while brittle fracture surfaces presented a smooth zone (Fig. 16c). This behavior is coherent with the findings of other authors who characterized

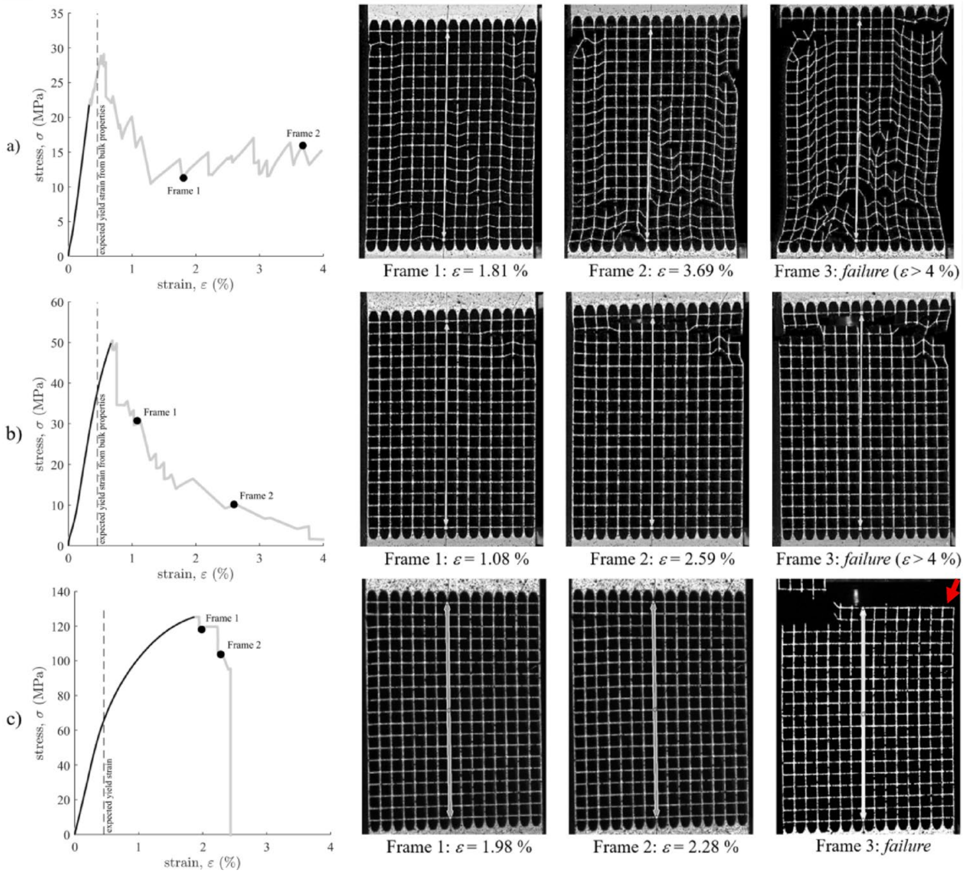

Fig. 15 Tensile stress–strain curves of IN718 samples with different wall thicknesses (t) and solid material proportions (P_s). Black lines indicate data up to the first local rupture; gray lines show full test duration. Panels correspond to: **a** t = 0.108 mm, P_s = 0.0558 (low thickness); **b** t = 0.130 mm, P_s = 0.0665 (medium thickness); and **c** t = 0.170 mm, P_s = 0.0870 (high thickness). Selected Digital Image Correlation (DIC) frames visualize deformation stages

IN625 alloy processed by PBF-LB/M [68]. Some areas showed dimples-like features (Fig. 16g), which probably are provoked by δ-phase and/or metal carbides (Fig. 16g), previously detected on grain boundaries, debonded due to the plastic deformation. The crack initiation could not be detected due to the complex fracture behavior of a grid-like structure even if various crack propagation paths are clearly visible (Fig. 16d, e). The majority of the crack growth directions were perpendicular to the load direction (Fig. 16e) but some of them are parallel to it Fig. 16d (left). Figure 16f, g, h show the dimples and microvoids typical of a ductile fracture surface. The dimple seems to be a preferred path for the crack propagation (Fig. 16d, right). Microstructural defects like pores do not seem to be responsible for the crack initiation. The crack initiation seems to be related to different wall thicknesses, P_s values, and the associated subjected stress.

3.4.2 Equivalent Young's modulus

Figure 17 shows the final evaluation regarding EYM of AlSi7Mg0.6 and IN718 samples. Dashed black lines represent the approximated EYM values that were expected for the grid structures by applying the proportion of areas between the region of the grid and the solid region based on literature EYM values for bulk materials. In addition, a more precise approach is represented by solid black lines (simulation reference) corresponding to the numerical EYM results obtained by means of FEA, which consider the stiffening effect of the transverse walls.

In general, samples showed an elastic modulus close to that predicted by the simulations for both, non-surface-treated and surface-treated samples. With regard to this aspect, the mean values of the different AlSi7Mg0.6 sample types showed a higher scatter than in the case of the IN718 samples. The thinnest samples, and especially AlSi7Mg0.6 samples, showed a noticeably lower EYM value, which may be associated with the larger relative influence of the defects as thickness decreases. However, IN718 samples with the same proportion showed EYM values close to those of the bulk material, which may indicate less defects present in the latter material. The applied surface treatment did not have any additional noticeable effect on the EYM apart from its direct influence on wall thickness and P_s, which directly affect the macroscopic mechanical response of the structure.

The results of the present study confirm that overall, the values of the elastic moduli of bulk AlSi7Mg0.6 and IN718 reported in the literature are appropriate to approximate the elastic moduli of non-surface-treated and surface-treated AlSi7Mg0.6 and IN718 heat exchanger cores, respectively. Furthermore, approximation of the EYM for the thin-walled

Fig. 16 Fracture surface analysis of an IN718 tensile specimen with wall thickness $t = 0.170$ mm and solid material proportion $P_s = 0.0869$ after tensile failure. **a** and **b** Fracture surface micrographs at low magnification showing an irregular surface; **c** Fracture surface, in a different location of the sample, showing ductile and brittle fracture surfaces areas. The right micrograph is a magnification of the left one; **d** Micrographs of the fracture surfaces showing a crack propagation path (left) as well as microvoids and dimples at high magnifications (right); **e** Micrograph showing crack propagation paths perpendicular to the load direction; **f**, **g** and **h** Micrographs showing microvoids at high magnification in ductile fracture surfaces; specifically **g** highlights a dimple-like feature

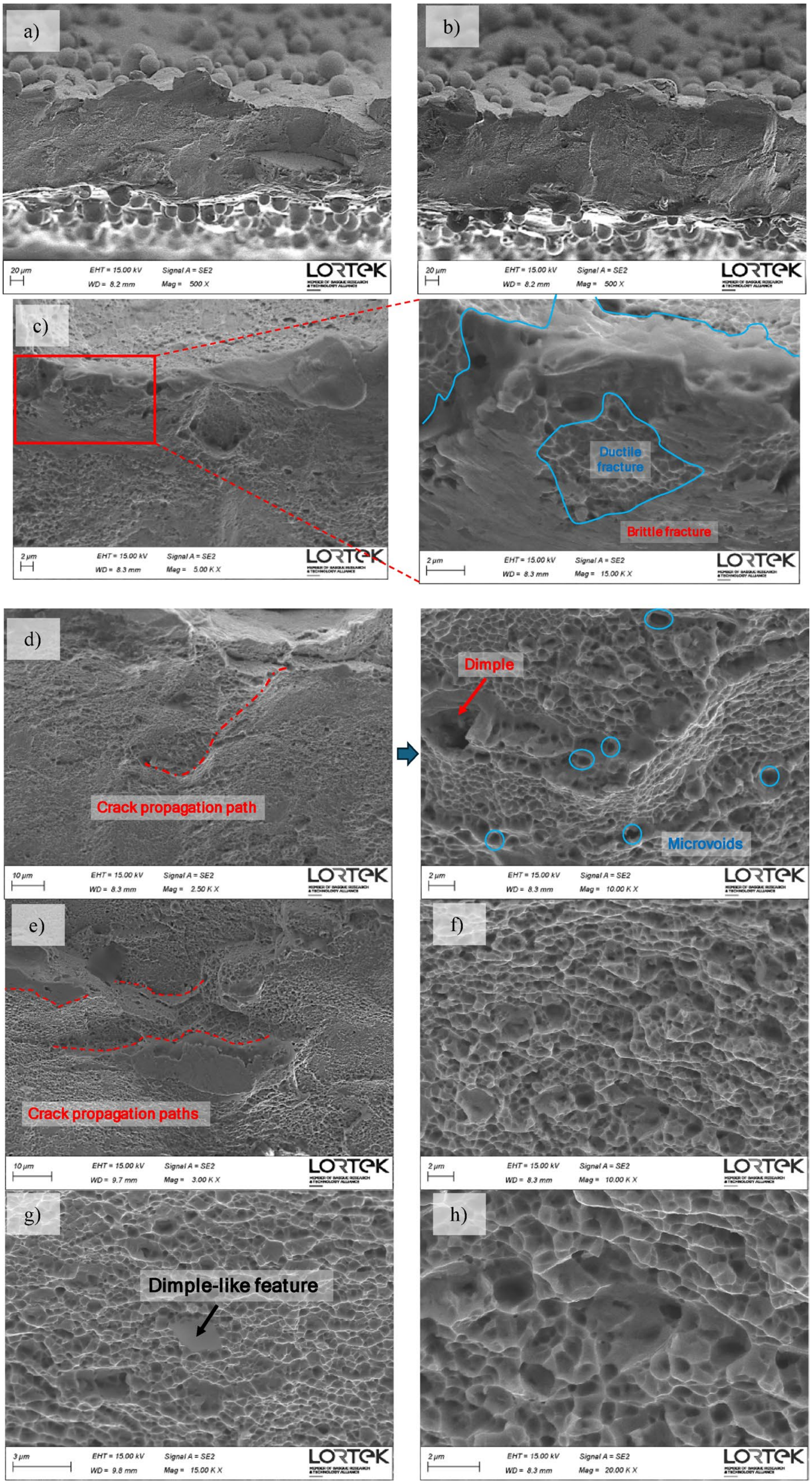

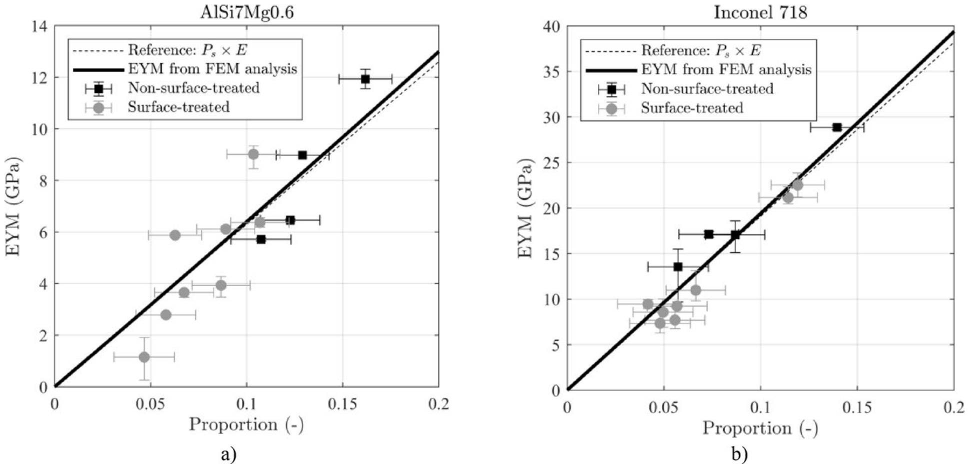

Fig. 17 Equivalent Young's moduli of AlSi7Mg0.6 (**a**) and IN718 (**b**) samples over proportion of non-surface-treated (■) and surface-treated (○) specimens compared to literature values for bulk materials (- - -) and the reference value from FEM simulation (——)

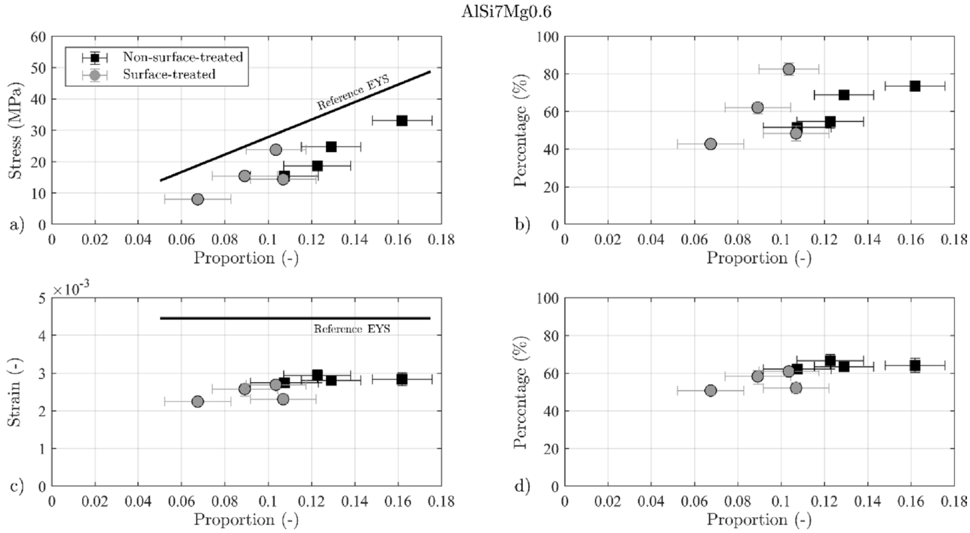

Fig. 18 Equivalent yield stress (**a**) and strain (**c**) of AlSi7Mg0.6 non-surface-treated (■) and surface-treated (○) specimens over proportion against the FEM simulation reference value (——), and the percentage (**b** and **d**) they represent with respect to the FEM simulation reference

structures by combination of bulk material values and the proportion of the thin-walled structure is reliable for the analyzed range. However, simulations should be considered in case wall thicknesses or proportions are used in heat exchanger design that exceed the values investigated in this study.

3.4.3 Equivalent yield strength

After analyzing the EYM, it is convenient to complement the information in Fig. 17 by showing the deformation capacity of the structures. For this purpose, the equivalent yield stress and equivalent yield strain achieved in the experiments are compared to the corresponding values obtained from the simulations. Simulated values are referred to as 'Reference' hereafter. The results are expressed as percentages relative to these reference values. The values are depicted over the proportion in Figs. 18 and 19 for AlSi7Mg0.6 and IN718 samples, respectively. Before continuing, it is important to emphasize that only the results of the samples that did show minimal plastic deformation before breaking have been plotted. Some of the thinner specimens broke within the elastic range, e.g., the samples shown in Figs. 13a and 15a, but the maximum stress at break cannot be considered as the yield stress, hence they have been omitted. Specifically, this happened in four references in the case of AlSi7Mg0.6 and in three in the case of IN718, as will be discussed more extensively later on.

As can be seen in Figs. 18 and 19, the ability to deform elastically differed significantly from expectations. In the case of AlSi7Mg0.6 alloy the ability to deform elastically was slightly greater as the thickness increased, but a percentage of about 60% of the expected deformation capacity was achieved in the best scenario (Fig. 18d). In IN718 samples (Fig. 19d), similar or slightly lower percentage values were achieved than in AlSi7Mg0.6. In both materials, larger dispersion was also noticed in the lowest proportion range. This is especially noticeable in the case of IN718 for which, unlike AlSi7Mg0.6, thinner samples also became plastically deformed. Furthermore, the surface treatment did not have

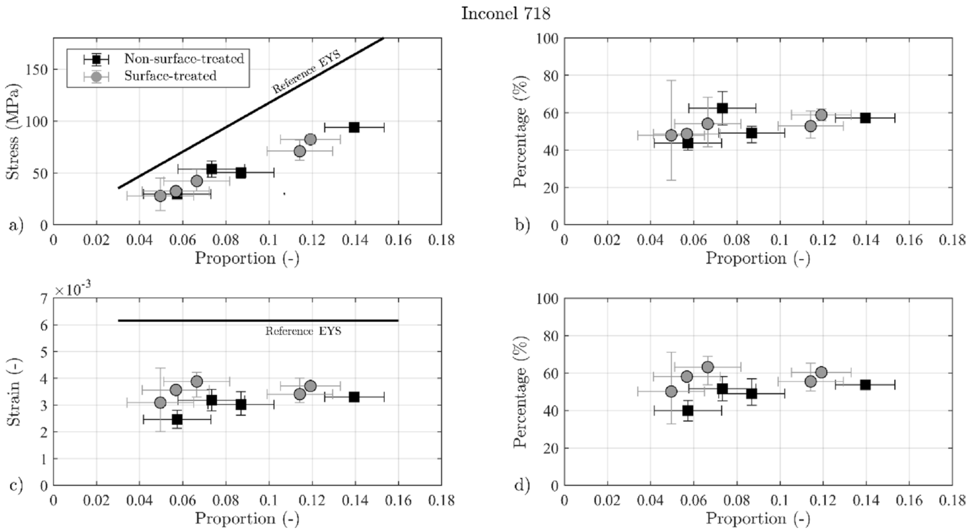

Fig. 19 Equivalent yield stress (**a**) and strain (**c**) of IN718 non-surface-treated (■) and surface-treated (○) specimens over proportion against the FEM simulation reference value (—), and the percentage (**b** and **d**) they represent with respect to the FEM simulation reference

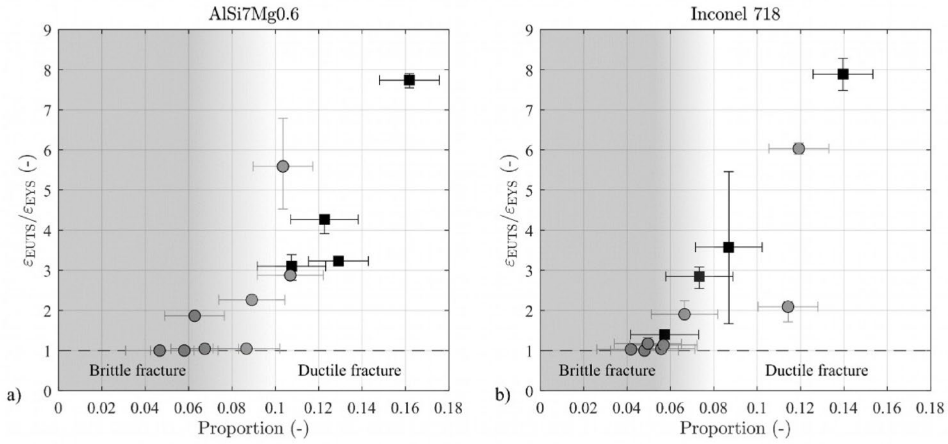

Fig. 20 Ratio between the equivalent strain at failure and the equivalent yield strain for AlSi7Mg0.6 (**a**) and IN718 (**b**) samples over proportion of non-surface-treated (■) and surface-treated (○) specimens

any additional noticeable effect on the capacity to deform elastically apart from its direct influence on wall thickness and P_s which in turn have an influence on the EYS. Finally, the greater repeatability of the results for the AlSi7Mg0.6 specimens is worth mentioning, showing a smaller dispersion (vertical error bars) than that shown by the results for the IN718 samples.

Plastic deformation occurred before reaching the equivalent elastic limit found in simulations. This was previously shown when discussing the failure mode in Figs. 13 and 15, and is also represented in Figs. 18 and 19. Moreover, some of the thinnest samples broke even before showing any macroscopic plastic deformation. A complementary indicator to discern between samples that showed macroscopic plastic deformation before breakage and those that ruptured without doing so, is presented next. In Fig. 20, the ratio between the strain at failure and yield strain is represented as a function of the proportion. Values close to one indicate no macroscopic plastic deformation before rupture, while increasing values indicate greater macroscopic plastic deformation before breakage.

As concluded from Fig. 20, the thinnest samples were more likely to break before undergoing plastic deformation due to the larger relative influence of defects. It can be seen that from proportion values around 0.06 onwards, IN718 always shows a minimum capacity to deform plastically, whereas in the case of AlSi7Mg0.6 the tendency is not so evident, requiring values above 0.09 for guarantying plastic deformation prior to failure.

These results, together with the EYM values, completely describe the elastic behavior of the samples. Next, the EUTS is discussed.

3.4.4 Equivalent ultimate tensile strength

To conclude characterizing the equivalent mechanical properties of thin-walled lattice structures, Figs. 21 and 22 show the EUTS of AlSi7Mg0.6 and IN718 samples, respectively. Specifically, the EUTS and strain at failure, and the

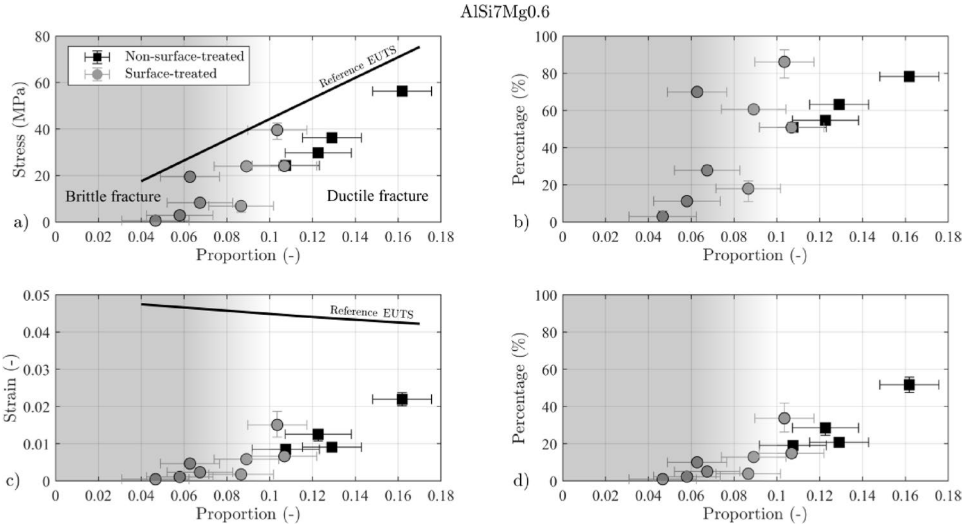

Fig. 21 Equivalent ultimate tensile stress (**a**) and strain (**c**) of AlSi7Mg0.6 non-surface-treated (■) and surface-treated (○) specimens over proportion against the FEM simulation reference value (──), and the percentage (**b** and **d**) they represent with respect to the FEM simulation reference. Additionally, the figure provides information on the observed fracture modes (brittle or ductile)

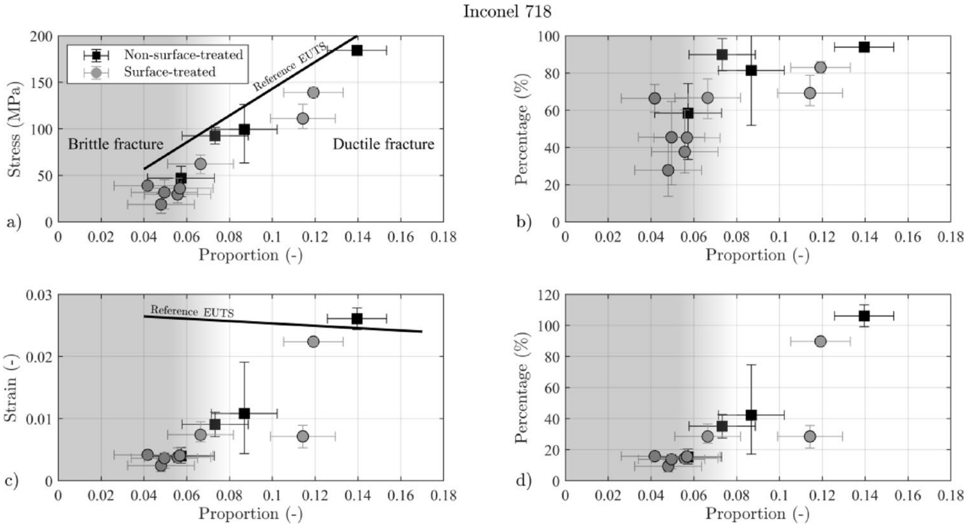

Fig. 22 Equivalent ultimate tensile stress (**a**) and strain (**c**) of IN718 non-surface-treated (■) and surface-treated (○) specimens over proportion against the FEM simulation reference value (──), and the percentage (**b** and **d**) they represent with respect to the FEM simulation reference. Additionally, the figure provides information on the observed fracture modes (brittle or ductile)

percentage they represent relative to the simulation values, are depicted.

As it is shown, samples showed lower EUTS values than the expected ones, especially for AlSi7Mg0.6, which showed lower percentage values with respect to the simulation reference than IN718. In the case of AlSi7Mg0.6, only for proportions above 0.09 did all investigated sample types consistently exceed 50% of the reference EUTS value (Fig. 21b). In contrast, for IN718, this occurred at proportion values above 0.06 (Fig. 22b). Above this proportion threshold, the IN718 exhibited higher EUTS, four specimen types reaching values between 80 and 90% of the reference value (Fig. 22b). In the case of AlSi7Mg0.6, however, only one specimen type reached above 80% of the simulation reference (Fig. 21b). Although stress levels near the reference were achieved in the best cases (Figs. 21b and 22b), the deformation capacity was significantly lower than predicted by simulations (Figs. 21d and 22d).

In the lower proportion range, rupture occurred without appreciable plastic deformation, as it is also shown in Fig. 20. Likewise, in the case of AlSi7Mg0.6, only the thickest specimen type exceeded 50% of the expected deformation capacity, but remained below 60% (Fig. 21d). In the case of IN718, larger deformation capacities were observed, reaching 90% and 106% for the two specimens with highest P_s values (Fig. 22d). Once again, no remarkable differences in EUTS values were observed between the non-surface-treated and surface-treated specimens.

3.5 Development of homogenized material models

Finally, homogenized material models are developed to predict the tensile mechanical response of the grid structures manufactured in AlSi7Mg0.6 and IN718. One possible approach was to develop models analogous to the studies on conventionally manufactured PFHE based on the homogenization method as presented in the introduction of this article. However, the development of such models requires extensive efforts beyond the scope of the present study. Another approach for modelling geometrically complex structures is given by the Gibson–Ashby model [69], which is the predominant model used to predict the properties of cellular structures, including lattices [70]. Therefore, in this section, first the applicability of the Gibson–Ashby model is examined to assess its ability to capture the effective mechanical properties of the structures under investigation. While the derived models prove suitable for estimating the EYM and EYS based on relative density or wall thickness ratios, they fall short in reproducing the strain-hardening behavior and ultimate failure in the plastic regime. To address these limitations, a novel homogenized material model based on the Hockett–Sherby law is proposed, in which the constitutive parameters are systematically defined as functions of the geometric wall thickness ratio. This approach enables an accurate and continuous representation of the stress–strain response across the full deformation range, including plastic flow and failure.

3.5.1 Gibson–Ashby model

The Gibson–Ashby model is a well-established model originally developed to describe the effective mechanical properties of cellular solids and foams as a function of their relative density. The Gibson–Ashby model is especially useful in the early stages of design of lattice structures manufactured via PBF-LB/M [70]. It is widely used to predict the homogenized elastic modulus, yield strength, and sometimes the collapse stress of structures exhibiting regular or stochastic porosity. The model assumes that each strut of the lattice is slender beam [71]. However, the model was also successfully used in the past for modelling of TPMS lattice structures that are not strut-based [70]. The model assumes that the mechanical response of the cellular solid can be captured through power-law relationships with respect to the relative density, with exponents that depend on whether the structure is bending- or stretching-dominated [71].

The model is classically derived for periodic architectures in three dimensions, such as open- or closed-cell foams, where the load-bearing elements are arranged in repeating units along all three spatial directions. Its formulation relies on the assumption of uniform load distribution across the periodic cells, and it may lose accuracy when the geometry or the dominant deformation mechanisms deviate from this periodic idealization. The lattice structures investigated in the present work exhibit periodicity in only two directions (corresponding to the in-plane arrangement of vertical and horizontal walls) while the third direction remains unstructured, allowing through-thickness transparency and airflow. This 2D or quasi-2.5D periodicity deviates from the assumptions of full 3D periodicity inherent in the Gibson–Ashby model, and may result in different load distribution mechanisms, particularly under uniaxial tension.

In order to apply the Gibson–Ashby formulation to the tested thin-walled structures, we introduce a geometric parameter that is more directly correlated with the structural stiffness and strength: the cross-sectional areas ratio or proportion (P_s). While the original model uses relative density as the independent variable, in this particular architecture the relative density scales linearly with wall thickness due to the constant number and spacing of the walls. As a result, the wall thickness ratio serves as a physically equivalent and more convenient parameter that directly controls the mechanical response. This substitution preserves the conceptual framework of the Gibson–Ashby model while enabling its application to structures where porosity is introduced through variations in wall thickness rather than cell size or spacing.

Despite the geometric limitations, we apply the Gibson–Ashby relations using this wall thickness-based formulation to determine the EYM and EYS, fitting them to power-law expressions. Experimental results are used to identify the corresponding exponents, allowing us to assess the validity and accuracy of the model in describing our anisotropic and partially periodic lattice geometry.

The Gibson–Ashby model, establishes power-law relationships between the effective properties of the porous structure and those of the fully dense base material. In its classical form, the model predicts the EYM, E_{eq} of the lattice structure as functions of the proportion:

$$E_{\text{eq}} = C_E E_{\text{bulk}} P_s^n \tag{4}$$

After fitting the model to the experimental EYM values, the coefficient was found to be $C_E = 1$, the exponent $n = 1$ reflecting the already observed linear relationship in Fig. 17. This outcome highlights the convenience of expressing the scaling law in terms of the cross-sectional area ratio or proportion P_s, since using relative density as the scaling parameter would lead to a value of $C_E \neq 1$, thereby reducing the simplicity and direct applicability of the formulation.

Similarly, the equivalent yield strength $\sigma_{\text{y,eq}}$ of the lattice structure as functions of proportion is given by

$$\sigma_{\text{y,eq}} = C_\sigma \sigma_{\text{y,bulk}} P_s^m \tag{5}$$

For the yield stress model, the fitting procedure resulted in a coefficient $C_\sigma = 0.59$ for AlSi7Mg0.6 and $C_\sigma = 0.52$ for the IN718. The exponent for both materials was $m = 1$, as was the exponent n, so the yield strain predicted by the Gibson–Ashby model is constant, the equivalent yield strain being defined as

$$\varepsilon_{\mathrm{y,eq}} = \frac{\sigma_{\mathrm{y,eq}}}{E_{\mathrm{eq}}} = \frac{C_\sigma}{C_E} \varepsilon_{\mathrm{y,bulk}} P_s^{m-n} \tag{6}$$

In Fig. 23 the fitting of the Gibson–Ashby model to the experimental data is depicted. The figure also delimits the brittle and ductile failure regions, the latter being the region where it could only be applied according to the results obtained in the present work.

The Gibson–Ashby model proved useful for predicting two key parameters that characterize the elastic behavior of the tested samples: the EYM and the yield strength. Both properties exhibited a linear relationship ($n = m = 1$) with respect to the proportion P_{s}, and the coefficient C_σ was determined for each material.

However, this applies only to the elastic range and is not valid for describing the plastic behavior, such as the ultimate tensile strength and material hardening. For this reason, in this work, a modified version of the Hockett–Sherby constitutive material model previously used is proposed, in which the coefficients are expressed as a function of the proportion.

3.5.2 Modified Hockett–Sherby model

To accurately capture the plastic region of the stress–strain curves of the thin-walled structures considered in this study, the Hockett–Sherby model already presented in Eq. (2) is proposed with a modified formulation in which its coefficients are expressed as functions of the cross-sectional area proportion, P_{s}. The modified Hockett–Sherby model is therefore defined as follows:

$$\sigma = \sigma_0\left(P_{\mathrm{s}}\right) + \left(\sigma_{\mathrm{s}}\left(P_{\mathrm{s}}\right) - \sigma_0\left(P_{\mathrm{s}}\right)\right)\left(1 - \mathrm{e}^{-m(P_{\mathrm{s}})\varepsilon^{n(P_{\mathrm{s}})}}\right) \tag{7}$$

Among the four coefficients, the initial yield stress σ_0 is already defined by the Gibson–Ashby model discussed in the previous section; therefore, only three coefficients needed to be identified. The three parameters were identified by minimizing the error between the experimental and predicted stress–strain curves by the Nelder–Mead simplex algorithm implemented in Matlab [72]. The fitting procedure was conducted in two distinct phases. In the first phase, the error between the experimental and predicted stress–strain curves was minimized simultaneously across all specimens with the same proportion P_{s}, in order to obtain averaged parameter values representative of their collective mechanical response. Following this, the dependence of the fitted parameters on the proportion was examined. A clear linear trend was observed for all three parameters, motivating a second phase of minimization. In this second phase, the error was minimized across all specimens that exhibited measurable plastic deformation, while enforcing a linear dependence of the three parameters on the proportion. This allowed for the direct identification of parametric equations valid within the studied range of proportions.

The resulting expressions for the four parameters of the modified Hockett–Sherby model are summarized in Table 8.

Another characteristic observed in the tensile behavior of the tested thin-walled specimens was their limited ductility prior to failure, which was significantly lower than that predicted by the FEM models. To incorporate this observation into the model, a linear function was fitted to the strain at failure values plotted as a function of the proportion, as

Fig. 23 Equivalent yield stress and strain of AlSi7Mg0.6 (**a** and **c**) and IN718 (**b** and **d**) non-surface-treated (■) and surface-treated (○) specimens over proportion against the FEM simulation reference value (──), and the one predicted by the fitted Gibson–Ashby model (- - -). Additionally, the figure provides information on the observed fracture modes (brittle or ductile)

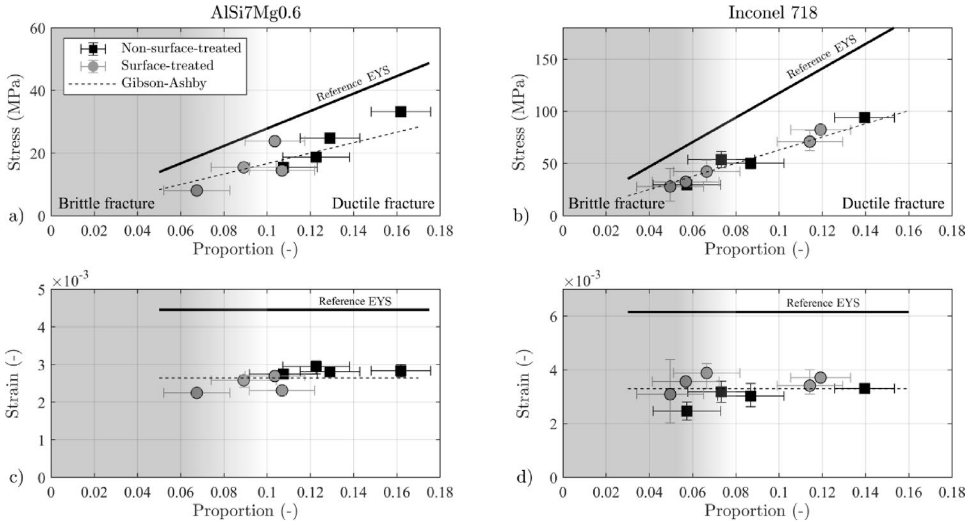

Table 8 Modified Hockett–Sherby parameters identified for AlSi7Mg0.6 and IN718 manufactured via PBF-LB/M

	AlSi7Mg0.6	IN718
Initial yield stress σ_0 [MPa]*	$0.59P_s$	$0.52P_s$
Steady-state flow stress σ_s [MPa]	$598.15P_s-30.63$	$918.46P_s+45.51$
Saturation coefficient m	$-50.14P_s+17.43$	$8769.1P_s-297.6$
Saturation exponent n	$-2.95P_s+0.964$	$0.1737P_s+1.18$

*Characterized by the Gibson–Ashby model

Table 9 Equations describing the strain at failure in function of proportion for AlSi7Mg0.6 and IN718 manufactured via PBF-LB/M

	AlSi7Mg0.6	IN718
Strain at failure	$0.1694P_s-0.0086$	$0.2124P_s-0.0073$

shown in Figs. 21 and 22. The resulting equations describing the expected strain at failure as a function of the proportion are presented in Table 9.

Finally, the validity of the fitted coefficients was assessed by comparing the stress–strain curves predicted by the modified Hockett–Sherby model with the corresponding experimental data. These comparisons are shown in Fig. 24 for three representative proportions spanning the full range investigated in this study.

As can be seen in Fig. 24, the modified Hockett–Sherby model together with the Gibson–Ashby model for determining the yield stress, and the third correlation for estimating the strain at failure, provide reliable predictions offering the following key points when designing thin-walled structures such as those analyzed in this paper.

One of the key findings is that the proposed model provides a realistic estimate of the yield strength, which is approximately 59% of the nominal value for AlSi7Mg0.6 and 52% for IN718. This information is crucial for the design of these structures, as it allows engineers to define safe loading limits that ensure the structure remains in the elastic regime during operation. In the event that the structure undergoes plastic deformation, the proposed model provides a more accurate prediction of both the strain at failure and the maximum load the structure can withstand. Additionally, it offers an improved representation of strain hardening throughout the plastic regime.

For both materials analyzed, the experimental stress–strain curves show significant deviations from those obtained through FEM simulations using the nominal bulk material properties reported in the literature. However, as the wall thickness increases, thereby increasing the proportion of load-bearing cross-sectional area, the experimental

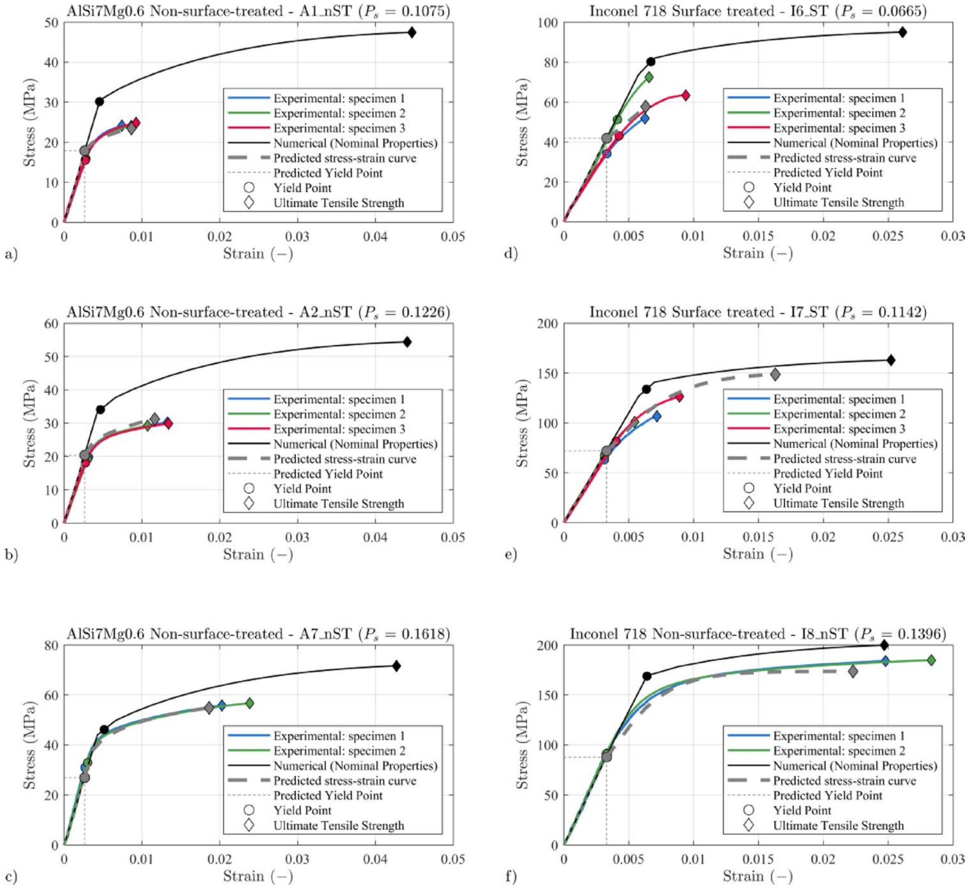

Fig. 24 Experimental stress–strain curves, yield point (●) and fracture point (♦), numerical counterparts obtained by the FEM model with nominal properties from literature, and the ones predicted with the proposed material model contemplating the proportion P_s for AlSi7Mg0.6 (a, b, and c) and IN718 (d, e , and f)

and predicted curves converge towards those obtained via FEM. This behavior is attributed to the greater influence of typical additive manufacturing defects (see Fig. 9) in thinner walls or lower proportions, an effect that the proposed material model accounts for to provide realistic predictions even for very thin-walled structures.

3.6 Additional considerations and limitations

The previously presented results give comprehensive insights into the mechanical properties of thin-walled grid-like structures in non-surface-treated and surface-treated condition manufactured in AlSi7Mg0.6 and IN718. Experimental data was compared to FEA and material models based on the Gibson–Ashby model as well as models based on the Hockett–Sherby constitutive model were developed for the investigated structures. While the results represent a valuable contribution to the field, it must be considered that uniaxial tensile tests in a single orientation of the thin-walled grid were performed in this study. This is associated with certain limitations concerning the applicability of the data. Furthermore, the reliability of the experimental results depends on the number of samples per sample type. The present data provide a basis for future studies with larger data sets. Additionally, no failure models were implemented in the FEA simulations when using the nominal bulk properties, which limited the reliability of the numerical results, particularly in the evaluation of EUTS. To address this, a new homogenized material model was proposed, demonstrating its ability to reliably predict both the hardening behavior and the equivalent ultimate tensile stress.

For more comprehensive insights into the mechanical response of the structure, a larger number of samples might be investigated as well as additional loads such as compression, shear, and torsion. Furthermore, the influence of the orientation of the grid structures under different loads could be studied. The results of this work represent a starting point for the efficient modelling of additively manufactured heat exchanger cores that consist of grid-like structures. The presented results do not allow for complex thermomechanical studies or creep fatigue life prediction that must be expected in many applications due to high temperatures and high pressures that are also necessary in heat exchanger design.

4 Conclusion and outlook

This study has explored the limits of additive manufacturing for the production of very thin-walled structures and has characterized their mechanical behavior in a previously unexplored range. The corresponding tensile test samples represent additively manufactured heat exchanger core structures, and their macroscopic mechanical properties, namely EYM, EYS and EUTS, were investigated. Samples were manufactured by PBF-LB/M in AlSi7Mg0.6 and IN718 and then heat-treated. Additionally, some of the samples underwent a surface treatment via chemical polishing. Tensile tests were performed using a DIC system to investigate stresses and strains in the thin-walled structures. Tensile tests of the designed samples were also simulated using finite element analyses. For data evaluation, the proportion of solid material in the predominant cross-sectional areas (P_s) was introduced as a comparative metric for the different thin-walled structures.

Regarding the failure mode, the AlSi7Mg0.6 and IN718 samples exhibited the expected elastoplastic deformation and breakage patterns only at proportion values above 0.09 and 0.06, respectively. For P_s values below these thresholds, mechanical properties were below expectations, with unpredictable fracture patterns and no noticeable plastic deformation occurring. It is probable that this phenomenon is attributable to the presence of common defects in the AM samples, which may exert a considerable influence on the macroscopic mechanical properties of the samples, particularly at low P_s values. The fractography analysis conducted in samples with wall thicknesses in the upper range, subscribes to a fracture mechanism involving both ductile and brittle behavior. It also reveals that defects of the microstructure do not lead to the crack initiation. Yet wall thickness seems to be more critical for fracture initiation.

For EYM, the experimental results for AlSi7Mg0.6 samples showed a greater deviation from the simulation reference values than those for IN718 samples. However, it was shown that both literature values for bulk materials as well as FEA are sufficient to predict the EYM of thin-walled structures within the analyzed ranges for both of the investigated materials.

Experimental results for EYS revealed that the samples began to undergo plastic deformation earlier than predicted by the simulations, likely due to defects acting as stress concentrators and reducing the effective load-bearing area. Overall, all samples of both materials exhibited EYS and strain values of approximately 59% of those predicted by the simulations for AlSi7Mg0.6, whereas for IN718 this value was slightly lower, around 52%.

For EUTS, experimental data was below simulation results for AlSi7Mg0.6 samples as well as IN718 samples. For AlSi7Mg0.6 with proportion values (P_s) above 0.09, while it is possible to achieve ultimate stress values at around 60–80% of those predicted by simulations, the structures' deformation capacity before fracture is significantly diminished. Only one AlSi7Mg0.6 sample type demonstrated a deformation capacity above 50%, with the remaining sample types achieving values below 40%. A similar conclusion is drawn for IN718. For IN718, it was observed that it is possible to achieve values of ultimate stress and strain at failure equivalent to those provided by simulations with lower proportions. Thus, above proportions of 0.14 the properties reported in the literature can be reliable to predict their mechanical behavior. Between 0.06 and 0.14, ultimate stress values of around 60–80% of those predicted by FEA may be achieved with a deformation capacity between 30 and 100%. Finally, reducing the proportion below 0.06, results in a significant deterioration of the properties. It is noteworthy that the chemical treatment designed to reduce roughness did not affect the mechanical properties of the material. Instead, the structure's properties were influenced only by the wall thickness. However, if a subsequent chemical treatment is anticipated, the reduction in thickness that the part will undergo must be considered during the design phase to ensure the expected mechanical performance. Furthermore, surface roughness is of great importance for the thermal and hydraulic characteristics of a heat exchanger and should be considered in its design.

Finally, homogenized material models have been proposed to characterize the tensile mechanical properties of the thin-walled structures, accounting for their deterioration as the wall thickness or proportion decreases. The Gibson–Ashby model is shown to be adequate for predicting the Equivalent Young's Modulus (EYM) and Equivalent Yield Stress (EYS) within the elastic range. To characterize the fracture load and strain hardening, a modified Hockett–Sherby model is proposed, and an additional correlation is presented to predict the fracture strain. The combination of these models proves effective in representing tensile mechanical behavior within the considered range of proportions.

Key findings:

- Reliable elastoplastic behavior occurs only above P_s values of ~ 0.09 (AlSi7Mg0.6) and ~ 0.06 (IN718); below these, brittle failure with no plastic deformation dominates.
- Experimental yield strength is about 59% (AlSi7Mg0.6) and 52% (IN718) of simulation predictions, due to the reduction of the effective load-bearing area and the stress concentration induced by the defects.
- Ultimate tensile strength and deformation capacity increase with solid proportion (P_s), but deformation capacity before fracture remains limited, especially for AlSi7Mg0.6.
- Surface polishing reduces roughness significantly but does not affect mechanical properties; wall thickness reduction due to polishing should be accounted for in design.
- Gibson–Ashby and modified Hockett–Sherby models accurately predict elastic and plastic tensile behavior as functions of P_s, enabling efficient and realistic mechanical property predictions for thin-walled AM structures.

The findings of this study enable more realistic predictions of the mechanical properties of thin-walled structures manufactured by PBF-LB/M in both AlSi7Mg0.6 and IN718. A methodology has been proposed to characterize the homogenized mechanical properties of very thin walls as a function of the proportion, which can be significantly affected by common defects inherent to additive manufacturing processes. This, in turn, allows for more accurate simulations of these structures, which is expected to be highly beneficial in the design of additively manufactured heat exchangers.

Appendix

See Table 10.

Table 10 Geometric parameters of experimental sample designs. "nST" and "ST" end of sample names stand for "non-surface-treated" and "surface-treated", respectively. Parameters L, b, m and A_T (Cross-sectional area, including voids) are according to the CAD files of the samples. Parameters a, d and t_{mean} were measured by caliper. Parameters c and A_{tw} (Cross-sectional area of thin wall, excluding voids) are based on t_{mean} and the CAD-file. Parameter P_s is based on A_{tw} and A_T

	Length of sample L [mm]	Length of clamping area b [mm]	Height of sample a [mm]	Width of sample d [mm]	Measuring length m [mm]	Avg. wall thickness t_{mean} [mm]	Avg. channel size c [mm]	Proportion of solid material in majorities of cross-sectional areas $P_s=A_{tw}/A_T$
AlSi7Mg0.6								
A1_nST	100.48	30	30.67	10.50	36.45	0.206	1.825	0.1075
A1_ST	100.48	30	30.52	10.39	36.45	0.089	1.940	0.0467
A2_nST	100.95	30	31.05	10.52	36.90	0.238	1.816	0.1226
A2_ST	100.95	30	30.91	10.39	36.90	0.112	1.941	0.0580
A3_ST	100.95	30	31.32	10.39	36.90	0.132	1.947	0.0674
A4_nST	105.70	30	34.84	10.52	41.40	0.281	2.023	0.1290
A4_ST	105.70	30	34.68	10.40	41.40	0.136	2.167	0.0627
A5_ST	101.43	30	31.77	10.41	37.35	0.172	1.935	0.0866
A6_ST	101.90	30	31.77	10.48	37.80	0.177	1.929	0.0891
A7_nST	105.70	30	34.90	10.48	41.40	0.353	1.950	0.1618
A7_ST	105.70	30	34.78	10.40	41.40	0.225	2.079	0.1035
A8_ST	101.90	30	31.74	10.38	37.80	0.212	1.890	0.1069
IN718								
I1_nST	100.76	30	30.70	10.33	36.72	0.110	1.929	0.0573
I1_ST	100.76	30	30.66	9.88	36.72	0.080	1.959	0.0417
I2_ST	100.76	30	30.66	10.45	36.72	0.092	1.946	0.0480
I3_ST	101.14	30	30.98	10.49	37.08	0.096	1.963	0.0496
I4_nST	101.14	30	31.01	10.45	37.08	0.142	1.916	0.0733
I4_ST	101.14	30	31.01	10.33	37.08	0.108	1.952	0.0557
I5_ST	101.14	30	30.99	9.75	37.08	0.110	1.949	0.0568
I6_nST	101.52	30	31.31	9.99	37.44	0.170	1.906	0.0869
I6_ST	101.52	30	31.29	9.75	37.44	0.130	1.947	0.0665
I7_ST	100.57	30	31.66	10.23	36.54	0.226	1.870	0.1142
I8_nST	100.57	30	34.74	10.08	36.54	0.303	1.993	0.1396
I8_ST	100.57	30	34.64	10.02	36.54	0.258	2.034	0.1192

Acknowledgements Part of this work results from the project "AManECO—Assessment of additive manufacturing limits for eco-design optimization in heat exchangers". This project has received funding from the Clean Sky 2 Joint Undertaking (JU) under grant agreement No 864733. The JU receives support from the European Union's Horizon 2020 research and innovation programme and the Clean Sky 2 JU members other than the Union. The article reflects only the authors' views and the JU is not responsible for any use that may be made of the information it contains. Furthermore, the authors would like to thank the Institute of Polymers and Composites of Hamburg University of Technology for their support during tensile testing and DIC measurements.

Author contributions Tim Röver: Conceptualization, Methodology, Validation, Formal Analysis, Investigation, Writing—Original Draft, Writing—Review & Editing, Visualization, Supervision, Project administration. Brian Biluh: Methodology, Validation, Formal Analysis, Investigation. Dirk Herzog: Conceptualization, Methodology, Validation, Writing—Review & Editing, Supervision, Project administration, Funding acquisition. Emma Gil: Methodology, Investigation, Resources, Writing—Review & Editing, Funding acquisition. Ane Miren Mancisidor: Methodology, Investigation, Resources, Writing—Review & Editing. Jon Aranzabe: Methodology, Investigation, Resources, Writing—Review & Editing. M.Belén García-Blanco: Investigation, Validation, Writing—Original Draft. Elixabete Espinosa: Investigation. Ephraïm Toubiana: Methodology, Writing—Original Draft. Leire Arrieta-Lizarazu: Investigation, Validation, Visualization, Writing—Review & Editing. Manex Martinez-Agirre: Formal Analysis, Writing—Original Draft, Writing—Review & Editing. Joanes Berasategi Arostegi: Formal Analysis, Writing—Original Draft, Writing—Review & Editing.

Funding Open Access funding enabled and organized by Projekt DEAL.

Data availability The raw and processed data required to reproduce the findings of this study are available upon request to the corresponding author. Please note that only certain data can be shared due to project restrictions; access to specific datasets will be granted accordingly.

Declarations

Conflict of interest The authors declare no conflict of interest.

References

1. van Heerden A, Judt DM, Jafari S, Lawson CP, Nikolaidis T, Bosak D (2022) Aircraft thermal management: Practices, technology, system architectures, future challenges, and opportunities. Prog Aerosp Sci 128:100767. https://doi.org/10.1016/j.paerosci.2021.100767
2. Sundén B, Fu J (2016) Aerospace heat exchangers. In: Fu J (ed) Heat transfer in aerospace applications. Elsevier Science Publishing Co, Ed., pp 89–115
3. Min JK, Jeong JH, Ha MY, Kim KS (2009) High temperature heat exchanger studies for applications to gas turbines. Heat Mass Transf 46(2):175–186. https://doi.org/10.1007/s00231-009-0560-3
4. Li J, Li Y (2023) Micro gas turbine: developments, applications, and key technologies on components. Propuls Power Res 12(1):1–43. https://doi.org/10.1016/j.jppr.2023.01.002
5. Zhang C, Gümmer V (2019) The potential of helicopter turboshaft engines incorporating highly effective recuperators under various flight conditions. Aerosp Sci Technol 88:84–94. https://doi.org/10.1016/j.ast.2019.03.008
6. Salpingidou C et al (2017) Thermodynamic analysis of recuperative gas turbines and aero engines. Appl Therm Eng 124:250–260. https://doi.org/10.1016/j.applthermaleng.2017.05.169
7. Yang X, Zhao W, Zhao Q, Xiang X, Hu B, Luo W (2024) Performance optimization for an advanced geared turbofan engine integrated with cooled cooling air heat exchangers. Energy 308:132718. https://doi.org/10.1016/j.energy.2024.132718
8. Liu Z, Xu G, Tang H, Wen J, Zhang J, Zhuang L (2025) Analysis of ultralow flow resistance heat exchangers on cooled cooling air and precooling technology. Appl Therm Eng 258:124760. https://doi.org/10.1016/j.applthermaleng.2024.124760
9. Kaur I, Singh P (2021) State-of-the-art in heat exchanger additive manufacturing. Int J Heat Mass Transf 178:121600. https://doi.org/10.1016/j.ijheatmasstransfer.2021.121600
10. Santos EC, Shiomi M, Osakada K, Laoui T (2006) Rapid manufacturing of metal components by laser forming. Int J Mach Tools Manuf 46:12–13. https://doi.org/10.1016/j.ijmachtools.2005.09.005
11. Saltzman D et al (2018) Design and evaluation of an additively manufactured aircraft heat exchanger. Appl Therm Eng 138:254–263. https://doi.org/10.1016/j.applthermaleng.2018.04.032
12. Hesselgraves JE, Law R, Reay DA (2016) Compact heat exchangers: selection, design and operation, 2nd edn. Butterworth-Heinemann, Amsterdam
13. Dib J, Lewon I, Martin B (2009) Thermo-mechanical design of brazed plate-fins heat exchanger based on finite element modeling using homogenization techniques. In Proceedings of the ASME Pressure Vessels and Piping Conference – 2009: Presented at 2009 ASME Pressure Vessels and Piping Conference, July 26–30, Prague, Czech Republic, Prague, Czech Republic, 2010. pp 21–27
14. Ge L, Jiang W, Wang Y, Tu S-T (2018) Creep-fatigue strength design of plate-fin heat exchanger by a homogeneous method. Int J Mech Sci 146–147. https://doi.org/10.1016/j.ijmecsci.2018.07.021
15. Ohno N, Narita K, Okumura D (2014) Homogenized elastic–viscoplastic behavior of plate-fin structures with two pore pressures. Int J Mech Sci 86:18–25. https://doi.org/10.1016/j.ijmecsci.2013.10.015
16. Jiang W, Gong JM, Tu ST (2011) Fatigue life prediction of a stainless steel plate-fin structure using equivalent-homogeneous-solid method. Mater Des 32(10):4936–4942. https://doi.org/10.1016/j.matdes.2011.05.048
17. Ge L, Jiang W, Zhang Y, Tu S-T (2017) Analytical evaluation of the homogenized elastic constants of plate-fin structures. Int J Mech Sci 134:51–62. https://doi.org/10.1016/j.ijmecsci.2017.09.041
18. Tsuda M, Takemura E, Asada T, Ohno N, Igari T (2010) Homogenized elastic–viscoplastic behavior of plate-fin structures at high temperatures: numerical analysis and macroscopic constitutive modeling. Int J Mech Sci 52(5):648–656. https://doi.org/10.1016/j.ijmecsci.2009.06.007
19. Hill R (1964) Theory of mechanical properties of fibre-strengthened materials: I. Elastic behaviour. J Mech Phys Solids 12(4):199–212. https://doi.org/10.1016/0022-5096(64)90019-5
20. Hill R (1963) Elastic properties of reinforced solids: some theoretical principles. J Mech Phys Solids 11(5):357–372. https://doi.org/10.1016/0022-5096(63)90036-X
21. Bensoussan A, Lions J-L, Lions, Papanicolaou G (1978) Asymptotic analysis for periodic structures. North-Holland Publ. Co, Amsterdam, New York, Oxford
22. Lene F, Leguillon D (1982) Homogenized constitutive law for a partially cohesive composite material. Int J Solids Struct 18(5):443–458. https://doi.org/10.1016/0020-7683(82)90082-8
23. Wu X, Ohno N (2002) A homogenization theory for inelastic behavior of materials with periodic internal structures. In: Bruhns OT, Stein E (Eds) Solid Mechanics and its Applications, IUTAM Symposium on Micro- and Macrostructural Aspects of Thermoplasticity. luwer Academic Publishers, Dordrechtpp, pp 187–196
24. Asada T, Ohno N (2007) Implicit formulation of homogenization method for periodic elastoplastic solids. KEM 340–341:1055–1060. https://doi.org/10.4028/www.scientific.net/KEM.340-341.1055
25. Bonneric M, Brugger C, Saintier N (2020) Effect of hot isostatic pressing on the critical defect size distribution in AlSi7Mg0.6 alloy obtained by selective laser melting. Int J Fatigue 140:105797. https://doi.org/10.1016/j.ijfatigue.2020.105797
26. Luo Z, Wang Z, Yan Z, Chen J, Li S, Liu M (2022) Formation of defects in selective laser melted inconel 718 and its correlation with mechanical properties through dimensionless numbers. Sci China Phys Mech Astron 65(5):254611. https://doi.org/10.1007/s11433-021-1861-1
27. Yang KV et al (2018) Porosity formation mechanisms and fatigue response in Al-Si-Mg alloys made by selective laser melting. Mater Sci Eng A 712:166–174. https://doi.org/10.1016/j.msea.2017.11.078
28. Celik E (2020) Additive manufacturing: science and technology. De Gruyter, Berlin, Boston
29. Yuan L et al (2020) Influence of structural features on processability, microstructures, chemical compositions, and hardness of selective laser melted complex thin-walled components. Int J Adv Manuf Technol 109:5–6. https://doi.org/10.1007/s00170-020-05773-1
30. Yuan L et al (2023) Laser additive manufacturing of microchannel array structure inspired by Lobster eyes: forming ability and optical focusing performance. Mater Sci Addit Manuf 2(2):361. https://doi.org/10.36922/msam.0361
31. Wan H, Chen H, Wang Y, Fang X, Liu Y, Kosiba K (2024) Laser additive manufacturing of Miura-origami tube inspired quasi-zero stiffness metamaterial with prominent longitudinal wave

propagation. Virtual Phys Prototyp 19(1). https://doi.org/10.1080/17452759.2023.2299691

32. Mantovani S, Giacalone M, Merulla A, Bassoli E, Defanti S (2022) Effective mechanical properties of AlSi7Mg additively manufactured cubic lattice structures. 3D Print Addit Manuf 9(4):326–336. https://doi.org/10.1089/3dp.2021.0176
33. Bogahawaththa M, Mohotti D, Hazell PJ, Wang H, Wijesooriya K, Lee CK (2024) Energy absorption and mechanical performance of 3D printed Menger fractal structures. Eng Struct 305:117774. https://doi.org/10.1016/j.engstruct.2024.117774
34. Zhang M, Bi G, Chen J (2024) Research on impact resistance of AlSi7Mg uniform and gradient porous structures manufactured by laser powder bed fusion. MSAM 3(4):5729. https://doi.org/10.36922/msam.5729
35. Kumar M, Garcia RM, Prasad S, Brochu M (2023) Evaluation of small-scale thin Wall AlSi7Mg alloys LPBF coupons under extreme low cycle fatigue regime, In: The 15th International Aluminium Conference. p 41
36. Liu C et al (2025) Research on comprehensive heat dissipation characteristics of AlSi7Mg TPMS heat sinks manufactured by laser powder bed fusion. Appl Therm Eng 261:124941. https://doi.org/10.1016/j.applthermaleng.2024.124941
37. Richter L et al (2024) Thermomechanical analysis of PBF-LB/M AlSi7Mg0.6 with respect to Rate-Dependent material behaviour and damage effects. Appl Mech 5(3):533–552. https://doi.org/10.3390/applmech5030030
38. Zea Pérez JM, Corona-Castuera J, Poblano-Salas C, Henao J, Hernández Hernández A (2022) On the manufacturability of Inconel 718 thin-walled honeycomb structures by laser powder bed fusion. RPJ 28(2):307–316. https://doi.org/10.1108/RPJ-04-2021-0098
39. Voyiadjis GZ, Abo Znemah R, Wood P (2023) Microstructure and geometry effects on the compressive behavior of LPBF-manufactured inconel 718 honeycomb structures. J Mater Res Technol 24:1562–1578. https://doi.org/10.1016/j.jmrt.2023.03.093
40. Xu Z, Tvenning T, Wu T, Razavi N (2024) Evaluating quasi-static and fatigue performance of IN718 gyroid lattice structures fabricated via LPBF: exploring relative densities. Int J Fatigue 178:108028. https://doi.org/10.1016/j.ijfatigue.2023.108028
41. Pauzon C et al (2022) Impact of contour scanning and helium-rich process gas on performances of alloy 718 lattices produced by laser powder bed fusion. Mater Desi 215:110501. https://doi.org/10.1016/j.matdes.2022.110501
42. Majeed M, Situ R, Javanbakht Z (2025) Effects of solution ageing in compressive behaviour of SLM-In718 triply periodic minimal surfaces. Prog Addit Manuf. https://doi.org/10.1007/s40964-025-01025-4
43. Srivathsan S, Ravichander BB, Shayesteh Moghaddam N, Swails N, Amerinatanzi A (2020) Investigation of the strength of different porous lattice structures manufactured using selective laser melting. In: Behavior and Mechanics of Multifunctional Materials IX, Online Only, United States, Apr 2020 - May. p 55. [Online]. Available: https://www.spiedigitallibrary.org/conference-proceedings-of-spie/11377/0000/Investigation-of-the-strength-of-different-porous-lattice-structures-manufactured/10.1117/12.2559106.full
44. Ananda V, Saravana Kumar G, Jayaganthan R, Srinivasan B (2022) Distortion prediction in Inconel-718 part fabricated through LPBF by using homogenized support properties from experiments and numerical simulation. Mater (Basel Switzerland) 15(17). https://doi.org/10.3390/ma15175909
45. Banait S, Jin X, Campos M, Pérez-Prado MT (2021) Precipitation-induced transition in the mechanical behavior of 3D printed inconel 718 Bcc lattices. Scripta Mater 203:114075. https://doi.org/10.1016/j.scriptamat.2021.114075
46. Gruber K, Ziółkowski G, Pawlak A, Kurzynowski T (2022) Effect of stress relief and inherent strain-based pre-deformation on the geometric accuracy of stator Vanes additively manufactured from inconel 718 using laser powder bed fusion. Precis Eng 76:360–376. https://doi.org/10.1016/j.precisioneng.2022.04.007
47. Vastola G, Sin WJ, Sun C-N, Sridhar N (2022) Design guidelines for suppressing distortion and buckling in metallic thin-wall structures built by powder-bed fusion additive manufacturing. Mater Des 215:110489. https://doi.org/10.1016/j.matdes.2022.110489
48. Yang H, Yang J, Huang W, Wang Z, Zeng X (2018) The printability, microstructure, crystallographic features and microhardness of selective laser melted inconel 718 thin wall. Mater Design 156:407–418. https://doi.org/10.1016/j.matdes.2018.07.007
49. Ahmed N, Barsoum I, Abu Al-Rub RK (2023) Numerical investigation of residual stresses in thin-walled additively manufactured structures from selective laser melting, *Heliyon*, vol. 9, no. 9, e19385. https://doi.org/10.1016/j.heliyon.2023.e19385
50. Wu T, Li C, Sun F, Liu PF, Xia HB (2024) Reduction in residual stress and distortion of thin-walled inconel 718 specimens fabricated by selective laser melting: experiment and numerical simulation. Int J Press Vessels Pip 212:105292. https://doi.org/10.1016/j.ijpvp.2024.105292
51. Wang W, Wang S, Zhang X, Chen F, Xu Y, Tian Y (2021) Process parameter optimization for selective laser melting of inconel 718 Superalloy and the effects of subsequent heat treatment on the microstructural evolution and mechanical properties. J Manuf Process 64:530–543. https://doi.org/10.1016/j.jmapro.2021.02.004
52. Golinveaux FS et al (2020) Fracture behavior of thin-walled inconel 718 manufactured with selective laser melting. In: AIAA Scitech 2020 Forum, Orlando, FL
53. Varney TC, Oldham T, Noor MI, Rottmann PF (2023) Quantifying the microstructure and mechanical property differences between bulk and Thin-wall additively manufactured inconel 718. Materialia 31:101867. https://doi.org/10.1016/j.mtla.2023.101867
54. Emanuelli L, Deirmina F, Pellizzari M (2023) Heat treatment behaviour of IN718 Superalloy fabricated by laser-powder bed fusion. Mater Charact 199:112788. https://doi.org/10.1016/j.matchar.2023.112788
55. Pereira JC, Gil E, Solaberrieta L, San Sebastián M, Bilbao Y, Rodríguez PP (2020) Comparison of AlSi7Mg0.6 alloy obtained by selective laser melting and investment casting processes: microstructure and mechanical properties in as-built/as-cast and heat-treated conditions. Mater Sci Engineering: A 778:139124. https://doi.org/10.1016/j.msea.2020.139124
56. ASTM B 918/B 918 Ma:2020: Standard practice for heat treatment of wrought aluminum alloys, American Society for Testing and Materials (ASTM), West Conshohocken, PA
57. DIN Deutsches Institut für Normung e. V (2019) https://doi.org/10.31030/3132591
58. Pei C, Shi D, Yuan H, Li H (2019) Assessment of mechanical properties and fatigue performance of a selective laser melted nickel-base Superalloy inconel 718. Mater Sci Eng: A 759:278–287. https://doi.org/10.1016/j.msea.2019.05.007
59. COMSOL, AB COMSOL Multiphysics - Reference Manual – 5.2a
60. Hockett JE, Sherby OD (1975) Large strain deformation of polycrystalline metals at low homologous temperatures, J Mech Phys Solids,23, no. 2, pp. 87–98. https://doi.org/10.1016/0022-5096(75)90018-6
61. COMSOL AB COMSOL Structural Mechanics Module - User's Guide – 5.2a
62. Malekipour E, El-Mounayri H (2018) Common defects and contributing parameters in powder bed fusion AM process and their

classification for online monitoring and control: a review. Int J Adv Manuf Technol 95:1–4. https://doi.org/10.1007/s00170-017-1172-6
63. Yadav P, Rigo O, Arvieu C, Lacoste E (2022) Microstructural and mechanical aspects of AlSi7Mg0.6 alloy related to scanning strategies in L-PBF. Int J Adv Manuf Technol 120:6205–6223. https://doi.org/10.1007/s00170-022-09127-x
64. Pereira JC, Aranzabe J, Taboada MC, Ruiz N, Rodriguez PP (2021) Analysis of microstructure and mechanical properties in As-Built/As-Cast and Heat-Treated conditions for IN718 alloy obtained by selective laser melting and investment casting processes. Crystals 11. https://doi.org/10.3390/cryst11101196
65. Gao Y et al (2019) Effect of δ phase on high temperature mechanical performances of inconel 718 fabricated with SLM process. Mater Sci Eng A 767. https://doi.org/10.1016/j.msea.2019.138327
66. Hitzler L et al (2020) Fracture toughness of L-PBF fabricated aluminium–silicon: a quantitative study on the role of crack growth direction with respect to layering. Prog Addit Manuf 5(3):259–266. https://doi.org/10.1007/s40964-020-00113-x
67. Paul MJ et al (2021) Fracture resistance of AlSi10Mg fabricated by laser powder bed fusion. Acta Mater 211:116869. https://doi.org/10.1016/j.actamat.2021.116869
68. Marchese G, Piscopo G, Lerda S, Salmi A, Atzeni E, Biamino S (2024) Heat-Treated inconel 625 by laser powder bed fusion: Microstructure, tensile Properties, and residual stress evolution. J Materi Eng Perform 33(13):6825–6834. https://doi.org/10.1007/s11665-024-09235-7
69. Gibson LJ, Ashby MF (2014) Cellular solids: structure and properties. Cambridge University Press
70. Maconachie T et al (2019) SLM lattice structures: Properties, performance, applications and challenges. Mater Des 183:108137. https://doi.org/10.1016/j.matdes.2019.108137
71. Zhong H, Song T, Li C, Das R, Gu J, Qian M (2023) The Gibson–Ashby model for additively manufactured metal lattice materials: its theoretical basis, limitations and new insights from remedies. Curr Opin Solid State Mater Sci 27(3):101081. https://doi.org/10.1016/j.cossms.2023.101081
72. Natick (2025) Massachusetts USA The MathWorks Inc. [Online]. Available: https://www.mathworks.com/products/matlab/whats-new-r2025a.html

Authors and Affiliations

Tim Röver[1] · Brian Biluh[1] · Dirk Herzog[1] · Emma Gil[2] · Ane Miren Mancisidor[2] · Jon Aranzabe[2] · M. Belén García-Blanco[3] · Elixabete Espinosa[3] · Ephraïm Toubiana[4] · Leire Arrieta-Lizarazu[5] · Joanes Berasategi Arostegi[5] · Manex Martinez-Agirre[5]

✉ Tim Röver
tim.roever@tuhh.de

Brian Biluh
brianbiluh@gmail.com

Dirk Herzog
dirk.herzog@tuhh.de

Emma Gil
egil@lortek.es

Ane Miren Mancisidor
ammancisidor@lortek.es

Jon Aranzabe
jaranzabe@lortek.es

M. Belén García-Blanco
bgarcia@cidetec.es

Elixabete Espinosa
eespinosa@cidetec.es

Ephraïm Toubiana
ephraim.toubiana@safrangroup.com

Leire Arrieta-Lizarazu
leire.arrietal@alumni.mondragon.edu

Joanes Berasategi Arostegi
jberasategui@mondragon.edu

Manex Martinez-Agirre
mmartinez@mondragon.edu

[1] Hamburg University of Technology, Hamburg, Germany

[2] LORTEK, Ordizia, Spain

[3] CIDETEC, Donostia-San Sebastián, Spain

[4] Safran (France), Paris, France

[5] Mondragon Unibersitatea, Arrasate-Mondragón, Spain